A MULTIMODALITY DLP® IMAGING SYSTEM

FOR CLINICAL SURGERY

by

MICHAEL LEE MANGUM

Presented to the Faculty of the Graduate School of

The University of Texas at Arlington in Partial Fulfillment

of the Requirements

for the Degree of

MASTER OF SCIENCE IN BIOMEDICAL ENGINEERING

THE UNIVERSITY OF TEXAS AT ARLINGTON

December 2011

ACKNOWLEDGEMENTS

This research project is a joint venture between the University of Texas at Arlington and the University of Texas Southwestern Medical Center at Dallas. I would first like to thank Dr. Karel Zuzak for giving me the opportunity to work in the Laboratory of Biomedical Imaging at the University of Texas at Arlington, and for his help mentoring me both academically and professionally. I would also like to thank Dr. Michel Saint-Cyr for his clinical guidance and patience while we imaged during his surgeries, and his positive energy as we worked to develop and tailor the system to his needs. I also really appreciate the help and support of Drs. Edward Livingston and Georgios Alexandrakis who helped to guide the project after Dr. Zuzak's transition to industry.

Furthermore, I would like to thank my labmates: Abhas Thapa and Eleanor Wehner for introducing me to the hyperspectral imaging systems and answering countless questions, Neil Jackson for his help in collecting clinical data, and Vatsala Rajanala and Naveenbalaji Balasubramanian for their additional help and support.

Major funding for this project was provided by Texas Instruments (TI), and I would like to thank all members involved, including Arun Chhabra, Dylan Thomas, Shekar Rao, and Jack Smith. I am also very appreciative of Maritoni Litorja and David Allen of the National Institutes of Standards and Technology, as well as Alex Fong of Gooch and Housego for their help answering questions and helping to accurately calibrate the imaging system.

Finally, I would like to thank my wife, Erin, for her support and patience through the long surgery days and late nights of data analysis as I completed this work.

November 22, 2011

ABSTRACT

A MULTIMODALITY DLP® IMAGING SYSTEM

FOR SURGICAL UTILITY

Michael Lee Mangum, M.S.

The University of Texas at Arlington

Supervising Professor: Edward H. Livingston

With 1.38 million new cases and 450,000 deaths worldwide due to breast cancer, there is a clear need for safe and complete surgical intervention for the treatment of breast cancer. Imaging solutions have been created and developed to help plastic surgeons during breast reconstructive surgery. However, these solutions were implemented separately depending on their particular modality, which can result in higher costs for hospital and patient use. The digital micromirror device (DMD) developed by Texas Instruments has been shown to exhibit spectral control of light at a digital level, and could theoretically allow for the incorporation of multiple imaging modalities into one system. Therefore, a DMD-based multimodality imaging system was developed to integrate both hyperspectral imaging and fluorescence angiography into a single system for use in clinical breast reconstruction surgery. The DMD-based light source was characterized to have a spectral resolution of less than 1 nm with full-width half-maximum bandwidths as small as 7.5 nm and total power output of up to almost 200 mW. This light source was integrated with a detector that is sensitive to

both visible and near-infrared light, along with a laptop computer with graphical user interface to control and synchronize the hardware. The resulting Mid-Range DLP® imaging system was found to be sensitive to changes in tissue oxygenation of skin flaps in DIEP free flap surgery using hyperspectral imaging of oxy-hemoglobin and deoxy-hemoglobin. Utilizing this imaging modality, plastic surgeons were able to visualize the distribution of tissue oxygenation to avoid necrosis of skin flaps used to reconstruct breast tissue. Furthermore, the Mid-Range DLP® imaging system was successfully able to fluoresce ICG in clinical surgery in patients with lymphedema in their upper extremity. The fluorescence angiography capability of this system allowed plastic surgeons to locate healthy lymphatic vessels used in lymphaticovenous bypass surgery in a non-invasive manner that would not otherwise be possible without the fluorophore.

TABLE OF CONTENTS

LIST OF ILLUSTRATIONS

Figure Page

LIST OF TABLES

Table Page

CHAPTER 1

INTRODUCTION

According to the World Health Organization in 2008, breast cancer was the most frequently diagnosed form of cancer in women, accounting for 1.38 million new cases and approximately 450,000 deaths worldwide.[1] Depending on prognosis, women can either undergo partial removal of the breast (lumpectomy) followed by radiation, or total removal of the breast (mastectomy) for treatment of the tumor.[2] Due to the invasive and disfiguring nature of the procedures, plastic surgeons deal with a myriad of problems in the operating room during breast reconstruction surgery.

During the lumpectomy or mastectomy, patients undergo sentinel lymph node biopsy or dissection to ascertain the stage and extent of the breast cancer. Unfortunately, this practice can result in damage to the lymphatic system at the axilla, resulting in accumulation of lymph in the upper extremity, a condition known as lymphedema. Lymphedema of the upper extremity can be very difficult to treat because plastic surgeons must bypass the damaged lymphatics by locating healthy lymph vessels that are on the order of ~3mm in diameter.[3] These vessels have no distinctive, distinguishing color relative to other tissue in the arm and can be very difficult to locate. Without the ability to discern where the lymph vessels are, plastic surgeons risk exacerbating the lymphedema by damaging the few remaining healthy lymphatics that have survived.

Indocyanine green (ICG) is a fluorophore first introduced in the late 1960s[4] that fluoresces in the near-infrared (NIR) wavelengths in what is considered the human body's "biological window" because it is not absorbed by other dominant chromophores like hemoglobin and melanin in the visible wavelengths or water in the NIR wavelengths above 900 nm.[5] Therefore, ICG can be detected

at greater depths in the body, and has been used to aid in measuring cardiac output [6], ophthalmology angiography, [7, 8] and more recently in plastic surgery for patients with lymphedema. [9] Technologies such as SPY and PhotoDynamics have created ICG angiographic imaging systems for vascular studies and patients with lymphedema for surgeons to better visualize the lymphatic system. [10, 11, 12]

Furthermore, during breast reconstruction surgery, autologous skin flaps are used to reconstruct the breast. For the plastic surgeon, the challenge is to balance "beauty and blood supply," meaning the autologous flaps should be large enough to create an aesthetically pleasing breast, but must also have enough blood supply to perfuse and oxygenate the entire flap. Assessing whether a particular skin flap has enough blood supply is not an easy challenge, and a surgeon sometimes has to rely heavily on clinical judgment. Companies, such as Vioptix, have employed hyperspectral fiber-based sensing of tissue oxygenation using near-infrared (NIR) spectroscopy to assess the vascularity of a free flap in breast reconstruction. [13]

Ultimately, each imaging solution is limited to its particular modality, which can also limit its application. Digital programming of light, through the use of DLP® technology created by Texas Instruments, allows for complete spectral control of an illumination, allowing the user to create narrow or broadband light of continuous or non-continuous spectra with varying intensity. Both ICG fluorescence and hyperspectral imaging of tissue oxygenation have been developed separately, but no one has integrated the imaging technologies, bringing multiple imaging tools to surgeons in a single imaging system. The research hypothesis is that the Mid-Range DLP® imaging system can successfully incorporate multiple imaging modalities into one system by employing both hyperspectral imaging and fluorescence angiography to aid plastic surgeons in breast reconstruction surgery.

This hypothesis will be proven, first, through a complete characterization of the imaging system's capabilities, followed by clinical studies in lymphaticovenous anastomosis surgery to aid in locating healthy lymphatic vessels, and in free flap breast reconstruction surgeries to help prevent

flap loss due to tissue necrosis. With incidence rates of cancer expected to rise due to increased awareness and early detection technologies, [14] the burden upon surgeons for complete and non-complicated treatment increases in parallel. Therefore, an integrated imaging system could serve as a very powerful tool to not only minimize the necessity for clinical judgment, but also improve the quality of patient care.

CHAPTER 2

SYSTEM CHARACTERIZATION

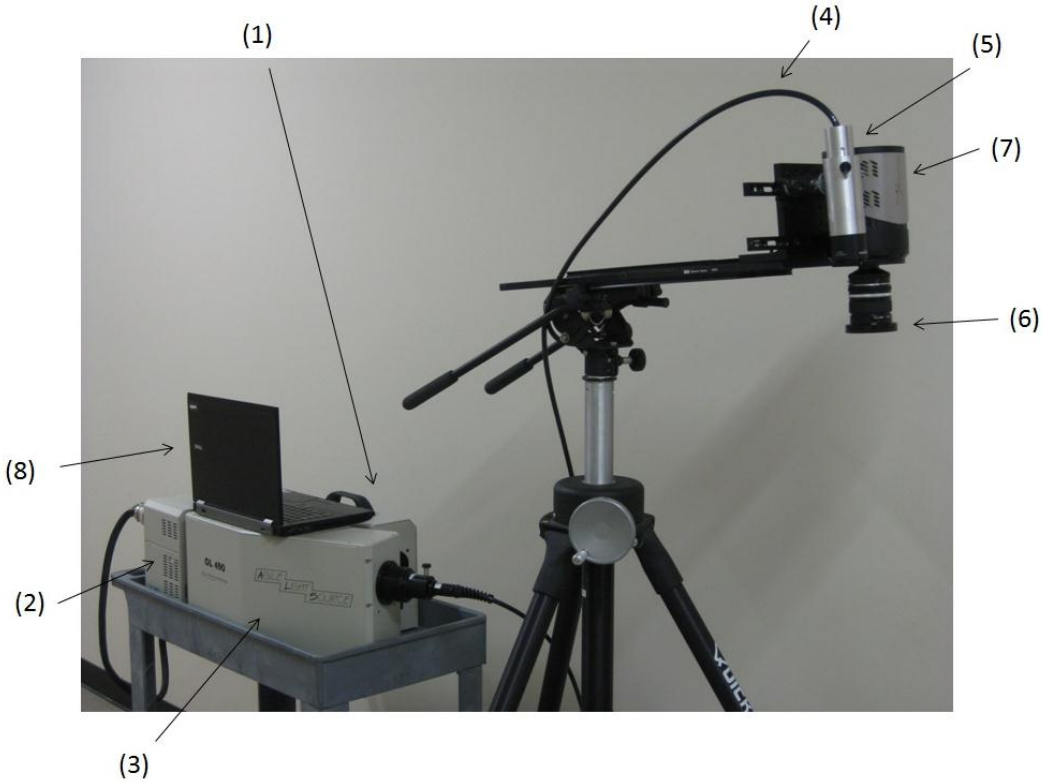

Figure 2.1 Mid-Range DLP® imaging system, consisting of a (1) radiometric power supply, (2) 500W xenon arc lamp, (3) DLP® controller, (4) 3mm liquid light guide, (5) custom adjustable beam-shaping optic, (6) Nikon wide-angle lens, (7) PIXIS camera detector, and (8) laptop computer.

The imaging system depicted in Figure 2.1 above, consists of a light source which utilizes Digital Light Projection (DLP®) technology developed by Texas Instruments to quickly and accurately shape light. The source is composed of a radiometric power supply (1), which powers a lamp (2), providing light to be shaped by the DLP® optics controller (3). This light is conveyed out of the source via a liquid light guide (4) and projected onto a region of interest using an adjustable beam-shaping optic (5). The resulting reflectance is measured with a lens (6) – detector (7) system,

and is transferred to a laptop (8) for image processing. The laptop computer provides a graphical user interface (GUI), as seen in Figure 2.2 that allows the user to manage and synchronize the hardware while also displaying the resulting image data. The entire system is made mobile by using a cart for the light source and a rolling tripod for the illumination optic and camera detector.

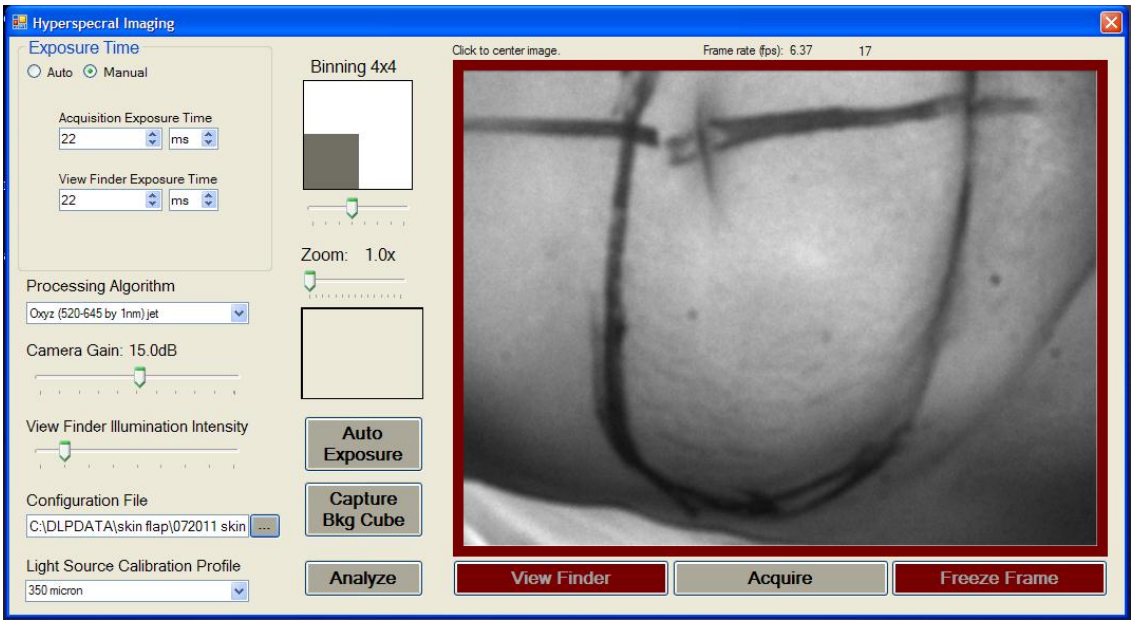

Figure 2.2 Graphical User Interface (GUI) for the DLP® Multimodality Imaging System

2.1. OL490 Agile Light Source

The multifunctional capabilities of this imaging system are primarily based on a dynamic light source called the OL490 Agile Light Source, developed and designed by Optronic Laboratories (now Gooch & Housego). The components of the OL490 and their proper operation have been described in detail elsewhere. [15, 16, 17] Briefly, the OL490 system consists of a radiometric power supply (S/N: 09101031) that provides stable power to a 500W Xenon arc lamp (S/N: 09002032). The lamp produces broadband, incoherent light that passes through one of four removable slits (150 µm, 350 µm, 500 µm, and 750 µm) before entering the DLP® optics controller (S/N: 09002028). Inside

the controller, coherent light is focused and passed through collimating optics before reaching a diffraction grating as indicated schematically in Figure 2.3.

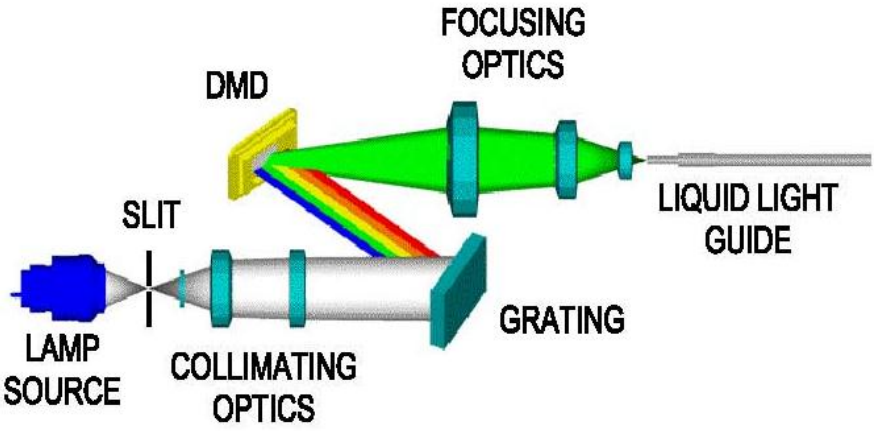

Figure 2.3 Schematic representation of the light path through the OL490 Agile Light Source.[18]

The 1-dimensional reflection grating separates light into its constituent wavelengths and projects them onto a DLP® digital micromirror device (DMD). The DMD is a 768 x 1,024 array of micro-mirrors mounted on a complementary metal-oxide-semiconductor (CMOS) substrate which electrically controls the pitch of the mirrors. The two positions, shown in Figure 2.4, illustrate the on/off positions for the mirrors when controlling the device's illumination. In the "off" position, light reflected off of the mirror is sent to a heatsink within the DLP® controller. In the "on" position, light is reflected into the exiting beam path and conveyed out of the device via a 3mm liquid light guide (LLG) (S/N: 09002028).

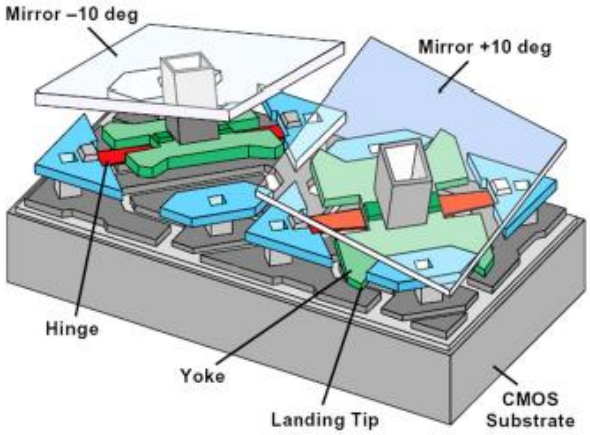

Figure 2.4 Two DMD pixels (mirrors shown as transparent) showing the on/off state of the mirrors.[19]

Light projected onto the DMD from the grating is one-dimensional, such that each column of mirrors corresponds to a single center wavelength of light. The intensity of each wavelength of light is controlled by the 768 mirrors within that column. Using this technology, one can individually control each mirror of the DMD to select bandpasses of light or create complex spectra of almost any desired illumination within the device's operating range. Optronic Laboratories (now Gooch & Housego) manufactured the OL490 Agile Light Source with three different wavelength ranges: a Visible system from 380 nm to 780 nm, a Near-Infrared (NIR) system from 760 nm to 1,600 nm, and a Mid-Range system from 525 nm to 1,050 nm. Because the Mid-Range system encompasses wavelengths of light pertinent to both biological tissue chromophores[5] and commonly used contrast agents like indocyanine green,[20, 21] it was chosen as the ideal light source for this multimodality imaging system.

2.2. Characterization of the Mid-Range OL490

2.2.1. Calibration of Measurement Devices

Prior to characterization of the imaging system, an Ocean Optics USB 2000+ spectrometer (S/N: USB2+F00577, Dunedin, FL) was first calibrated with irradiance and spectral sources optically certified by the National Institute for Standards and Technology (NIST). The USB 2000+

spectrometer has a spectral measurement range from 340 nm to 1,030 nm covering the 2,048 pixels of a Sony ILX511 16 bit charge-coupled device (CCD). Each pixel of the CCD corresponds to a specific center wavelength, covering almost the entirety of the manufacturer's specified operating range for the Mid-Range OL490 system. In order to properly characterize the OL490 light source and subsequent imaging illuminations, the spectrometer's wavelength accuracy and sensitivity to light were first verified with light sources of known spectral and irradiance responses, respectively.

2.2.1.1. Spectral Calibration of the Spectrometer

A NIST-traceable HG-1 Mercury Argon Calibration source (Ocean Optics, Dunedin, FL), with a wavelength range from 253 nm to 1,700 nm, was used to tune the spectrometer per manufacturer's specifications. A QP400-1-VIS/NIR 400 μm fiber (S/N: EOS-28082, Ocean Optics, Dunedin, FL) with an operating range from 400 nm to 2,500 nm was used as an interface between the light source and detector. Briefly, spectral peaks created by the calibration source were identified by the spectrometer's software and pixel values were recorded at each known peak. A linear regression was performed by Microsoft Excel (Microsoft, Redmond, WA) using the first, second, and third power of the recorded pixel values as three separate independent variables per manufacturer's instructions. These three variables were regressed in a single linear regression model to predict the actual wavelength values specified in the HG-1 lamp's calibration. The regression resulted in a coefficient of determination (R^2) of 99.99%, and the coefficients of the regression were programmed into the EEPROM of the spectrometer to properly adjust its spectral readings to the new calibration standard.

2.2.1.2. Irradiance Calibration of the Spectrometer

The USB 2000+ spectrometer's sensitivity to light was also characterized using a NIST-traceable AvaLight HAL-CAL irradiance source (S/N: 1005002, Avantes, Broomfield, CO) with a calibrated spectral output from 350 nm to 1,095 nm. The irradiance source was coupled to an ISP-400 2" integrating sphere (Thorlabs, Sterling, VA), as shown in Figure 2.5, to completely homogenize

the broadband source's output before being directed to the spectrometer via a QP400-1-VIS/NIR 400 μm fiber. This combination of integrating sphere, fiber optic, and spectrometer will be used in all subsequent experiments to yield measurements in International Standard (SI) units of microwatts per centimeter squared per nanometer ($mW/cm^2 \cdot nm$) based on the calibrated light source.

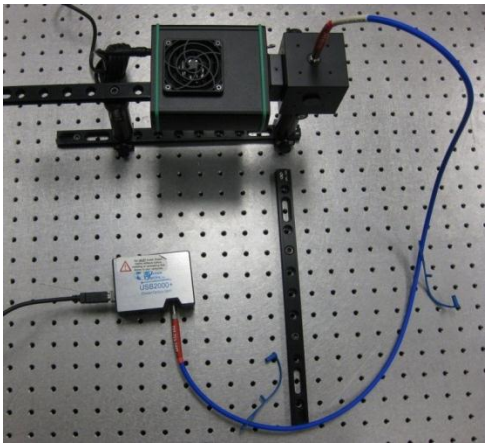

Figure 2.5 Measurement setup for irradiance calibration of the USB 2000+ spectrometer.

During future experiments, the spectrometer will measure a range of intensities of light. Therefore to ensure all signals are above the noise threshold but also not saturated, the integration time of the spectrometer will need to be adjusted appropriately. In general, CCDs, like the one found in the spectrometer, have an output voltage that is proportional to the amount of incident light. Therefore, for a light source of constant intensity, as integration time increases, the intensity counts measured by the spectrometer will also increase proportionally. However, each pixel of the CCD receives a different center wavelength of light, and therefore is not guaranteed to have the same response (in counts) for a given change integration time. In fact, Figure 2.6 shows the variability in the spectral sensitivity of the CCD's pixels as specified by the manufacturer.

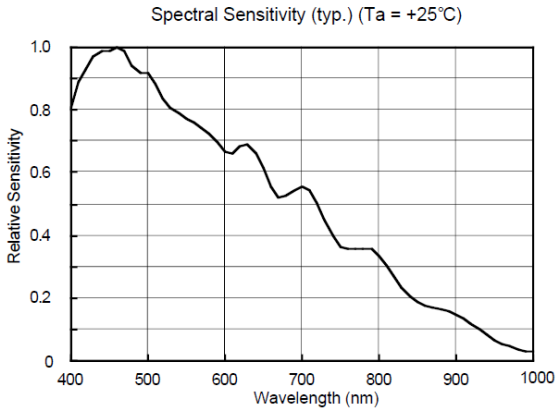

Figure 2.6 Manufacturer's specified spectral sensitivity of the Sony ILX511 CCD found in the Ocean Optics USB2000+ spectrometer.[22]

Because a pixel's sensitivity to incident light varies as a function of wavelength, each pixel on the spectrometer's CCD will have a unique change in counts due to a change in integration time. After allowing the HAL-CAL lamp to warm up for 15 minutes, the light source was measured at integration times ranging from 5 ms to 250 ms at different intervals (5 ms to 10 ms every 1 ms, 10 ms to 100 ms every 5 ms, and 100 ms to 250 ms every 10 ms). Counts measured at each center wavelength (pixel) of the spectrometer's CCD were divided by the known power of the light source at that wavelength to obtain a measure of counts per microwatt. The change in counts per microwatt as a function of integration time was measured using a linear regression for each individual pixel of the CCD. The coefficient of determination (R^2) of each linear regression was used as a metric of the validity of the regression model for use in calibrating future experiments. Over the spectral range of the USB2000+ spectrometer (340 nm - 1030 nm), pixels corresponding to wavelengths between λ = 386.06 nm to 1,030.7 nm had $R^2 \geq 90\%$, and wavelengths between λ = 422.38 nm to 1,030.7 nm had $R^2 \geq 99\%$. Therefore, between an integration time of 5 ms to 250 ms, and a wavelength range from λ = 422.38 nm to 1,030.7 nm, future light intensity measurements made with this experimental calibration setup, were recorded in SI units of watts per meter squared (W/m^2).

2.2.2. OL490 Experiment Preparation

To ensure accurate and repeatable results with the OL490 Agile Light Source one must take precautionary steps prior to each use. The lamp's warm up time and stability have been previously characterized in a thesis by R.P. Francis using a NIST-calibrated photodiode.[15] Stability was shown to have <1% standard deviation in day-to-day use, after the lamp was allowed to warm up for at least 15 minutes. Therefore, each time the system is used, the lamp is allowed to warm up for 15 minutes prior to data collection. Furthermore, because the lamp housing is separate from the DLP® optical controller, alignment of the lamp with the controller is crucial to obtaining accurate and repeatable measurements. Prior to each use, a spectrometer was used to measure the output from a single mirror column of the DMD. The middle column of the DMD, column 512, was turned 'on,' while all other columns were turned 'off,' per manufacturer's specification. The measured center wavelength of the resulting light was aligned with Optronic Laboratories' pre-programmed calibration of the same mirror column, using three set screws in the lamp housing to fine-tune any differences in alignment. These precautionary steps of lamp warm up and alignment were taken prior to any experimental or clinical data collection to help guarantee more accurate and repeatable results.

2.2.3. Irradiance

The irradiance of the Mid-Range OL490 Agile Light Source was measured for each of its four inter-changeable slits by interfacing the output of the LLG with the entrance port of the integrating sphere. Counts measured by the spectrometer were averaged over 10 acquisitions and converted into microwatts based on the previous calibration of the spectrometer. Dividing by the aperture area of the 400 μm fiber yielded the irradiance as a function of wavelength. Figure 2.7 shows the Mid-Range OL490's irradiance for each of the four slits. These results are significantly lower than the irradiance specified by Optronic Laboratories when they ship the OL490, as seen in Figure 2.8. However, this difference in light power is mostly attributed to the age of the lamp. OL's specifications

give the irradiance from a brand new lamp, whereas irradiance measurements of the Mid-Range system were made after the lamp had well over 100 hours of use.

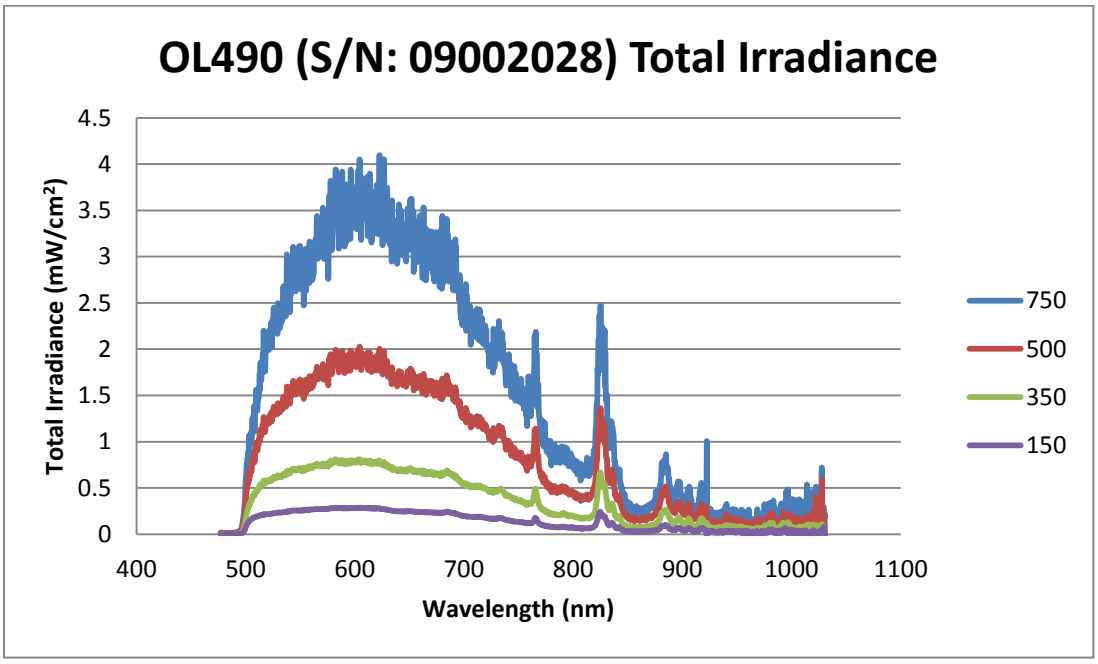

Figure 2.7 Measured irradiance of the Mid-Range OL490 (S/N: 09002028) with a lamp of 100+ hours

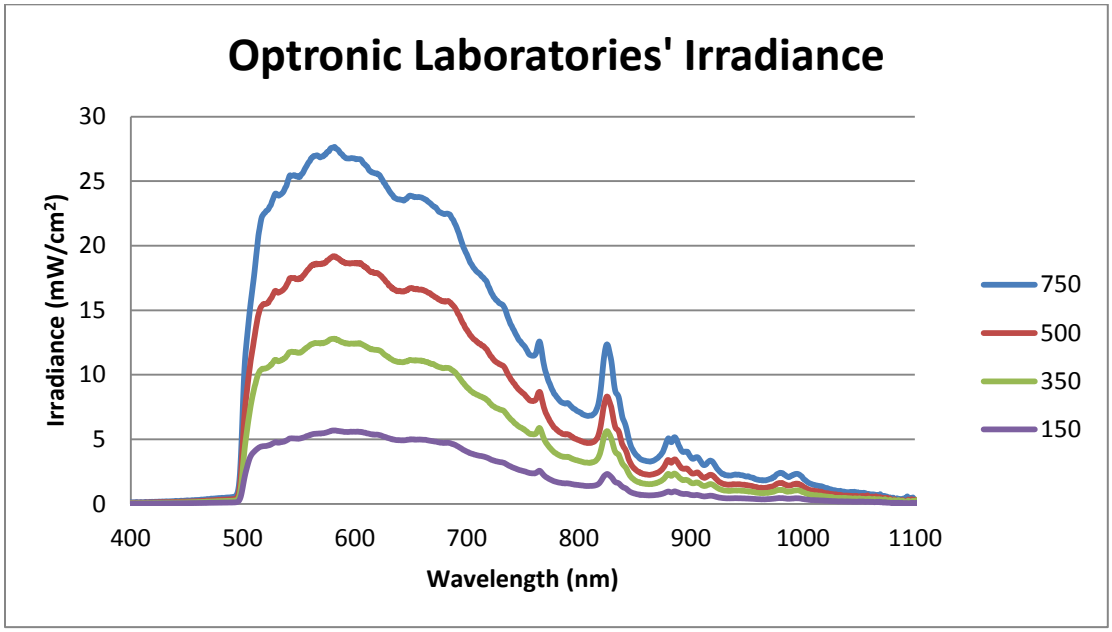

Figure 2.8 Irradiance of the Mid-Range OL490 as specified by Optronic Laboratories

There is a clear difference in the power output of the OL490 depending on the slit size chosen. As expected, larger slits allow for more light to enter the DLP® optic controller due to their larger aperture size. The total irradiance of the 750 μm, 500 μm, 350 μm, and 150 μm slits are 2,453.3 mW/cm^2, 1,349.9 mW/cm^2, 591.3 mW/cm^2, and 213.9 mW/cm^2, respectively, with a total power output of 173.4 mW, 95.4 mW, 41.8 mW, and 15.1 mW, respectively.

However, there is a tradeoff for using larger slits with more light. The larger aperture of the big slits allows for incident light to strike a larger area of the grating, which will cause a larger spatial dispersion of the diffracted spectra across the columns of the DLP® DMD. Figure 2.9 illustrates the idea of spatial dispersion off of a reflection grating. Incoherent collimated light is incident on the grating at an angle θ_i. Diffracted light reflects off of the grating grooves spaced a distance, a, apart. All of the diffracted light reflects at the same angle θ_m:

$$a \sin \theta_m = m\lambda$$

Equation 1

where a is the distance between two grooves, θ_m is the diffraction angle for the m order of diffraction, and λ is wavelength.

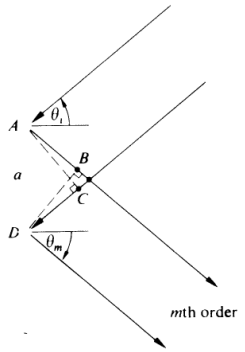

Figure 2.9 Diffraction of light on two adjacent grooves of a reflection grating. [23]

Because light reflected from the grooves of the grating travels parallel, when it reaches its destination at the mirrors of the DMD, it will still be separated by a distance a. Therefore, an increase

in the illuminated area on the grating, due to a larger slit, will cause a larger spatial dispersion of diffracted light across the DMD. Thus, although larger slits provide greater illumination intensity, they come at the cost of larger bandwidths of light for a given column of mirrors. This phenomenon could be corrected for with a focusing lens between the grating and DMD, but Gooch & Housego engineers confirmed that there was no focusing lens in place to decrease spatial dispersion. Other factors like chromatic and geometric aberrations inherent to any lens system, like the DLP® controller, could also contribute to the spatial dispersion of diffracted light onto the DMD. However, the major contribution to increased dispersion was confirmed by G&H engineers to be the lack of a focusing optic.

2.2.4. Mirror Recruitment

To better understand and confirm the dispersion of a single wavelength over multiple mirror columns, DMD mirrors were individually controlled using .GXT files. A single mirror column corresponding to a center wavelength of 576 nm was chosen for illumination. For each slit, the full-width half-maximum (FWHM) bandwidth and irradiance of a single mirror column, *c*, was measured first, then subsequent measurements recruited columns *c*+1 and *c*-1 to column *c* before collecting a second measurement. This process was repeated until the total number of mirror columns equaled 71 for each slit. Figure 2.10 shows the measured spectra as mirror columns were added to the original single mirror column at 576 nm.

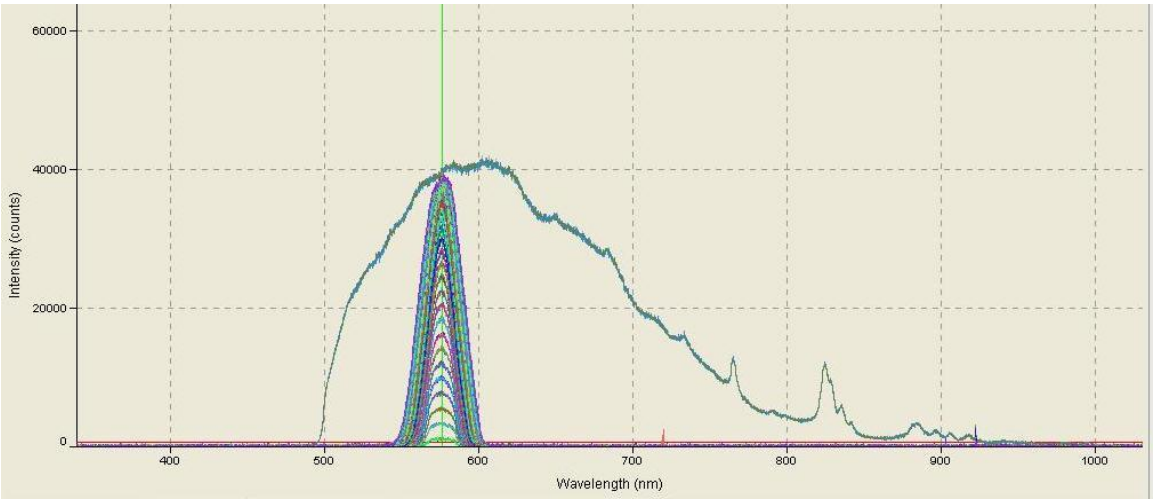

Figure 2.10 Mirror recruitment about a single center wavelength (576nm)

Initially, as mirror columns are recruited, the FWHM remains relatively constant while intensity increases. However, as more and more mirrors are recruited, the intensity at 576 nm begins to reach a plateau, and the FWHM begins increasing. This tradeoff between bandwidth and intensity is different for each slit of the OL490, and can be better visualized in Figure 2.11, where the solid lines correspond to the measured irradiance at 576 nm (left axis), and the dashed lines represent the FWHM measured at 576 nm (right axis). The minimum measured FWHM bandwidth for the 150 μm, 350 μm, 500 μm, and 750 μm slits was 7.51 nm, 12.96 nm, 18.96 nm, and 27.35 nm, respectively. This increase in FWHM bandwidth with increasing slit size is consistent with the geometrical constraints discussed previously. Furthermore, the larger 500 μm and 750 μm slits require more mirror columns to be recruited before reaching maximum intensity for a given wavelength. The 150 μm, 350 μm, 500 μm, and 750 μm slits, require 25, 33, 39, and 51 mirror columns to reach within 10% of their respective maximum intensities, again confirming the change in spatial dispersion of wavelengths of light over the columns of the DMD due to changing slit sizes.

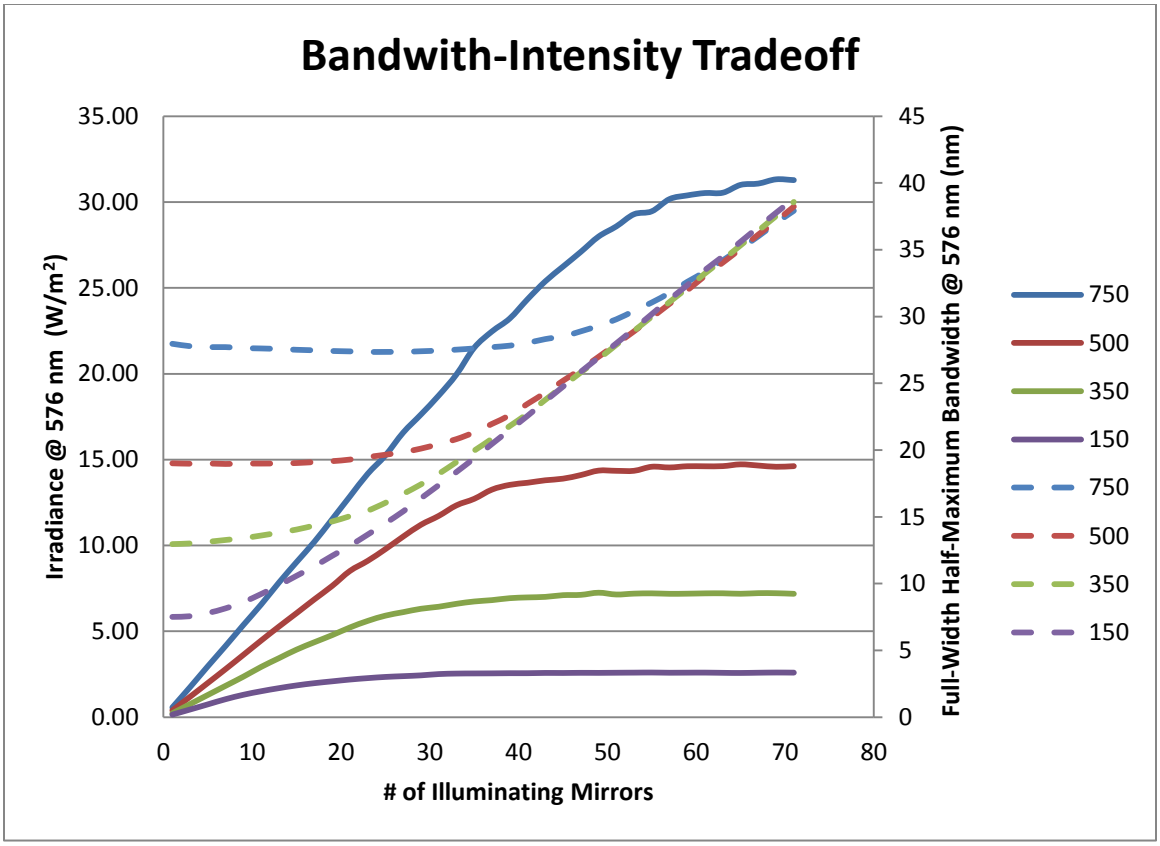

Figure 2.11 Bandwidth-intensity tradeoff based on the recruitment of mirror columns. Solid lines correspond to the irradiance measured (left axis), and dotted lines represent the full-width half-maximum (FWHM) bandwidth measured (right axis).

Interestingly, this examination has yielded some performance information that the end-user can take advantage of when shaping light. Note that, as the number of recruited mirror columns is increased for each slit, there is an initial period of approximately constant FWHM bandwidth before the bandwidth begins to increase. During this time, the spectral width and peak intensity of the light increases proportionally such that the FWHM bandwidth remains approximately constant at 576 nm, while the irradiance of the light increases. Therefore, the intensity of output light can be adjusted within this region without affecting FWHM bandwidth. For the 150μm slit, this period is very short before the FWHM bandwidth changes by 5% (5 mirror columns, corresponding to a range of 0.02 mW/cm^2 to 0.08 mW/cm^2). The larger slits, however, are capable of varying irradiance without changing FWHM bandwidth on a larger scale. The 350 μm, 500 μm, and 750 μm slits can vary

irradiance with ranges of 0.02 – 0.2 mW/cm^2, 0.04 – 1.05 mW/cm^2, and 0.06 – 2.80 mW/cm^2, respectively, without altering the FWHM bandwidth by more than 5%.

2.2.5. Spectral Accuracy

To determine the spectral accuracy of the OL490, single columns of the DMD were illuminated across the spectral range, and their output was measured by the integrating sphere, fiber, spectrometer setup from section 2.2.1.2. However, as the output light approached near-infrared (NIR) wavelengths, the signal was significantly attenuated and very noisy. Therefore, mirrors were recruited based on results from section 2.2.4 such that the bandwidth of the center wavelength did not increase by more than 5%, but the intensity was significantly larger to generate more signal for the spectrometer. Based on mirror recruitment measurements, 5, 11, 27, and 49 mirrors were recruited for the 150 μm, 350 μm, 500 μm, and 750 μm slits, respectively. Sweeps across the output range of the OL490 were generated based on the size of the mirror recruitment.

Table 2.1 Spectral accuracy of the Mid-Range OL490

Slit	***m* (slope)**	***b* (*y*-intercept)**	***R*^{2}**
750 μm	1.00	1.62	99.98%
500 μm	1.00	0.58	99.99%
350 μm	1.00	-0.88	100.00%
150 μm	1.00	-2.68	100.00%

The results in Table 2.1 show that, even after proper alignment of the lamp housing with the optics controller, there can still be a shift (variable *b*) between the measured output of the Mid-Range OL490 and the manufacturer's specification. These shifts in illumination were compensated for in illumination files to guarantee complete spectral accuracy.

2.2.6. Bandwidth Sweep

Using the same methods as section 2.2.5, the FWHM bandwidth was measured over the wavelength range of the Mid-Range OL490. Figure 2.12 shows that the FWHM bandwidth is relatively constant from 505 nm to 715 nm for each of the four slits. However, as the light transitions from visible to NIR wavelengths, the changes in bandwidth vary significantly from one mirror column to the next. This peculiar behavior can be partially attributed to the lamp profile seen in Figures 2.7 and 2.8, but mostly, the light output is severely attenuated, and therefore resulted in noisy measurements.

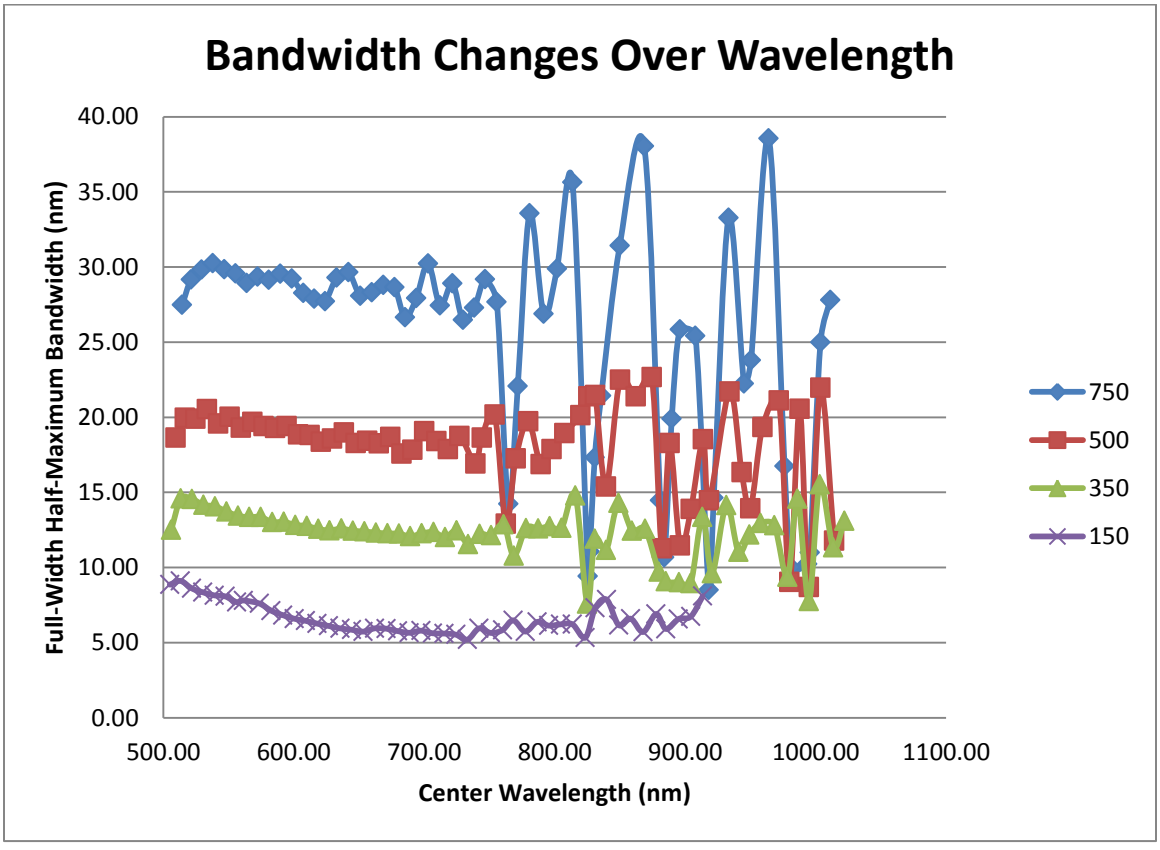

Figure 2.12 Spectral dependence of bandwidth over the wavelength range of the Mid-Range OL490

2.3. Adjustable Illumination Optic

To make this system more flexible and adaptable to different imaging environments, an adjustable illumination optic was designed and fabricated by the Laboratory of Biomedical Imaging at UTA. The goal was to design an optic that could concentrate the output light from the LLG of the OL490 onto a range of spot sizes, so that little light was wasted. Using an Olympus 110AL2X-2 WD38 (Hamburg, Germany) lens, a cylindrical housing was designed to hold and displace the end of the LLG relative to the Olympus lens. An exploded assembly view of the design can be seen in Figure 2.13 below.

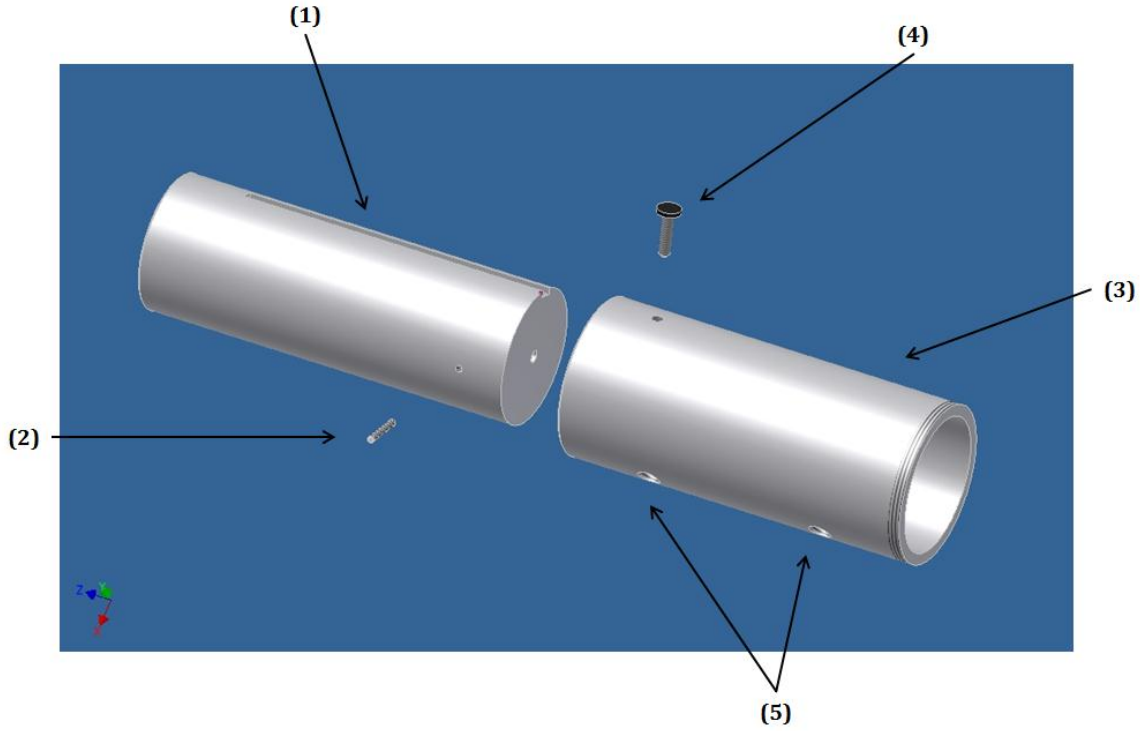

Figure 2.13 Exploded view of adjustable illumination optic consisting of the inner cylinder (1), small set screw (2), outer cylinder (3), large set screw (4), and ¼-20" tapped holes (5).

The outer cylinder (3) of the optic is threaded at the front to hold the Olympus lens, and has two ¼-20" taps (5) for mounting onto a tripod or other optics equipment. The inner cylinder (1) holds the front of the LLG flush with its face using a small set screw (2), then is made to displace relative to the outer cylinder along a groove. Larger spot sizes are created by bringing the LLG closer

to the Olympus lens, creating more incident angles of light exiting the optic. Conversely, moving the end of the LLG further away from the Olympus lens, decreases the incident angles of light exiting the optic, making a smaller spot size. Once a desired illumination target size is found, the large set screw (4) can be tightened to lock the two cylinders in place relative to each other.

2.3.1. Spot-Size Range

The adjustable illumination optic's range of spot sizes was evaluated at a distance of two feet from the target, since this is the minimum acceptable distance for imaging with non-sterile equipment in a surgical operating room. At two feet, the adjustable optic could create spot diameters as large as 26" (66.04 cm) and as small as 1 ¾" (4.45 cm).

2.4. PIXIS 1024BR Camera

Figure 2.14 Princeton Instruments PIXIS 1024BR detector

The PIXIS 1024BR camera detector made by Princeton Instruments (Trenton, NJ, S/N: 2910090005) has a spectral sensitivity that ranges from 350 nm to 1,050 nm, making it very useful for the Mid-Range OL490 light source. The detector utilizes a back-illuminated, deep depletion CCD that has a native resolution of 1,024 x 1,024 pixels. Each 13 μm x 13 μm pixel of the focal plane array can be digitized as a 16-bit integer at a rate of either 100 kHz or 2MHz. The choice in digitization

speed allows the user to select between high speed or low noise operation according to the manufacturer. However, the camera also employs thermoelectric air cooling to minimize dark current noise. Figure 2.15 depicts the manufacturer's specified quantum efficiency for the detector, stretching from ultraviolet (UV) to NIR wavelengths. Again, the sensitivity of the detector over both visible and NIR wavelengths makes it ideal for detecting both biological tissue chromophores [5] and commonly used contrast agents like indocyanine green, [20, 21].

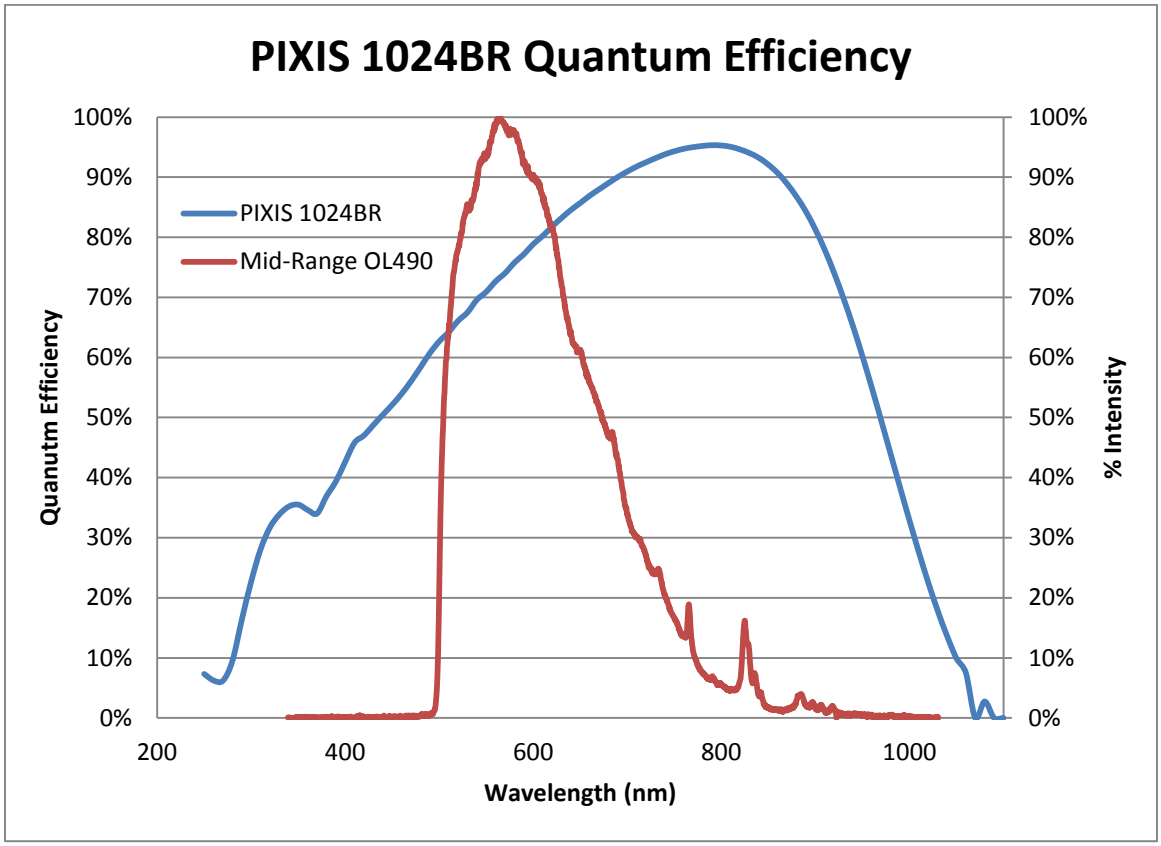

Figure 2.15 The manufacturer specified quantum efficiency of the PIXIS 1024BR detector and the % intensity output of the Mid-Range OL490 as a function of wavelength.

Despite the camera's spectral capabilities, it also needs to be able to capture high-quality, low-noise images at a fast rate to make the system viable in medical environments like a surgical operating room.

2.4.1. Speed & Image Noise

The speed and imaging noise of the camera was evaluated to determine the optimum parameters that produce high speed, quality images. A spatially uniform 12" square SRT-99-120 spectralon (Labsphere, North Sutton, NH) was imaged from a distance of two feet away. The entire viewing area of the CCD was filled by the spectralon, and the signal to noise ratio (SNR) was determined from Equation 2:

$$SNR = \frac{\mu_{signal}}{RMS\ noise}$$

Equation 2

where μ_{signal} is the mean image pixel intensity measured in counts, and *RMS noise* is the root-mean-square noise measured in counts, defined as:

$$RMS\ noise = \sqrt{\frac{\sum_{i=1}^{n}\left(X_i - \frac{\sum_{i=1}^{n} X_i}{n}\right)^2}{n}}$$

Equation 3

where X_i is the intensity counts of the *i*th pixel, and *n* is the total number of pixels in an image. The spectralon target was imaged for a total of 120 seconds, and the number of complete frames was tallied to determine the speed of the detector in frames per second (fps).

With the PIXIS 1024BR, there are three detector parameters that can be varied to improve the speed of the system at the potential cost of image quality. The exposure time, image binning, and gain, were all varied to see how the speed and SNR of the detector were affected. The f-stop on the focusing lens was used to balance the maximum intensity of the images to approximately 60,000 counts as each parameter was changed. While the use of the f-stop has its own compromises with depth of field, it would not affect the analysis because the lens was focused on the reflectance standard which is a flat target. Therefore, varying the f-stop was considered an effective method of balancing image counts while allowing for variation of the camera settings. Prior to image capture,

the camera was allowed to warm up for 30 minutes, and default values of the exposure time (20 ms), binning (1x1), and gain (1) were used when these parameters were not being tested.

2.4.1.1. Exposure Time

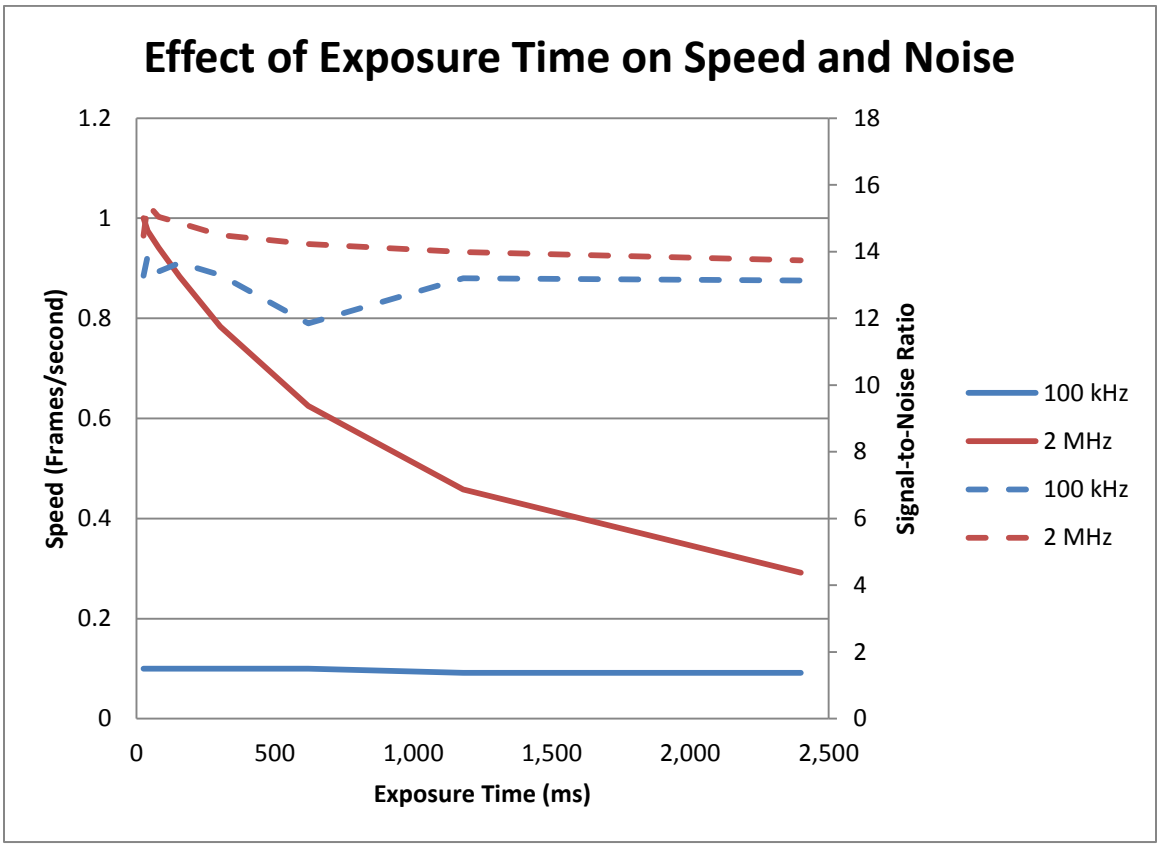

Figure 2.16 The change in speed and signal-to-noise ratio as a function of exposure time on the PIXIS 1024BR. Solid lines correspond to the left axis representing the speed of the detector, and dashed lines correspond to the right axis representing the signal-to-noise ratio.

The f-stop of the detector's lens was varied over a range from f/1.4 to f/16, which resulted in measurement of the speed and SNR of the detector over a range from 26 ms to 2,400 ms of exposure time. Figure 2.16 shows the change in speed (represented by solid lines) and the change in SNR (represented by dashed lines), as a function of exposure time for each digitization mode of the PIXIS 1024BR. The 2 MHz "speed" mode results in a maximum frame rate of 1 fps at 20 ms exposure and falls off quickly to 0.29 fps by 2,400 ms. Fortunately, the SNR of the images does not change drastically as exposure time is varied, and only drops from 15.4 to 13.7 over the range of exposure

times. The 100 kHz "low-noise" mode of the camera was measured to have lower dark current counts compared to the 2 MHz mode (626 vs. 711 counts, respectively), however, its SNR remained consistently below the 2 MHz digitization mode. Furthermore, as expected, the lower frequency digitization mode was slower than the 2 MHz mode, and was actually so slow, that any change in the exposure time over this range resulted in no change in capture speed. At 100 kHz digitization, the camera detector held a constant speed of 12 completed frames in 120 seconds, equaling 0.1 fps.

2.4.1.2. Binning

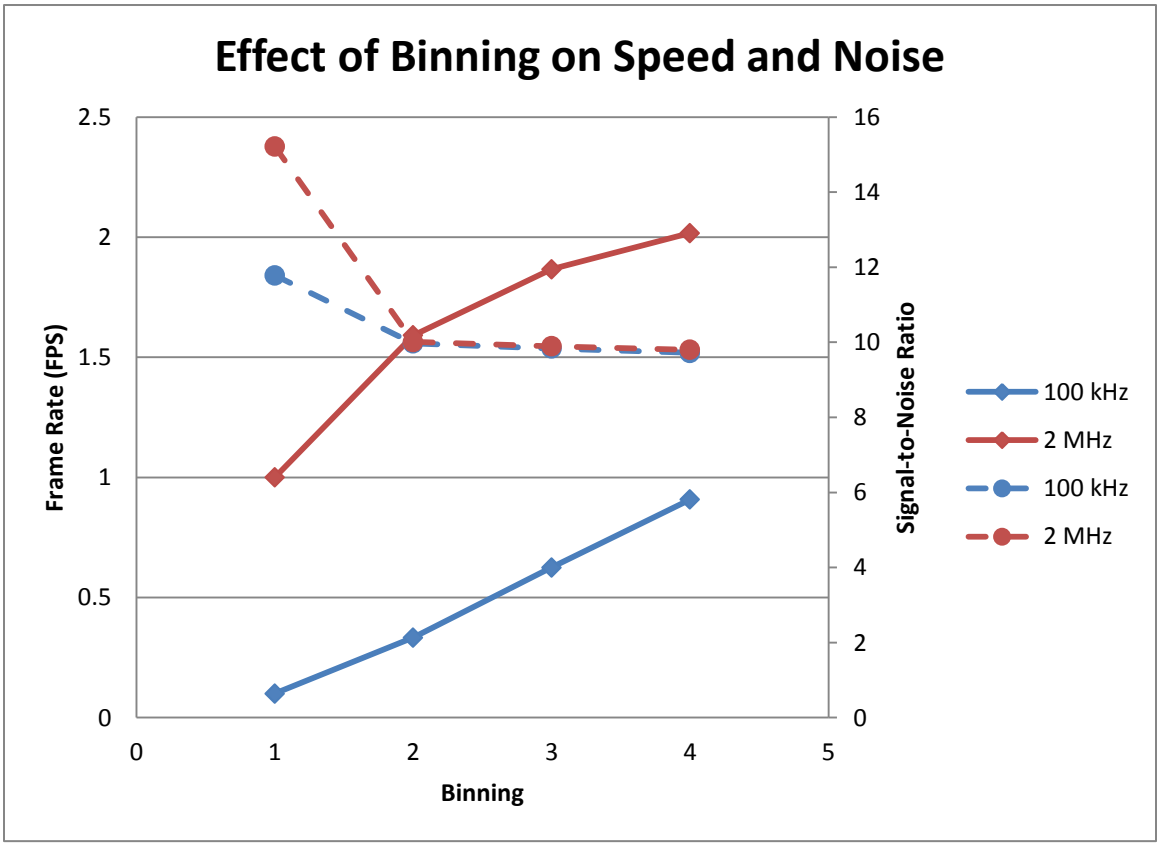

Figure 2.17 The change in speed and signal-to-noise ratio as a function of image binning on the PIXIS 1024BR. Solid lines correspond to the left axis representing the speed of the detector, and dashed lines correspond to the right axis representing the signal-to-noise ratio.

Imaging speed and SNR were also evaluated based on image binning modes. For the PIXIS 1024BR, the user has a choice of 1x1 (1,024 x 1,024 pixels), 2x2 (512 x 512 pixels), 3x3 (341 x 341 pixels), or 4x4 (256 x 256 pixels) binning modes. Binning allows for the additive combination of a

group of *n* x *n* pixels to form a single superpixel. This results in a reduced need for image intensity and exposure time, and further decreases the digitization time because there are less pixels to be processed. Figure 2.17 shows the change in speed (solid lines) and SNR (dashed lines) as a function of image binning for each digitization mode of the PIXIS 1024BR. Image binning significantly improves image speed for 100 kHz digitization, increasing it by a factor of 9 from 0.1 fps (1x1) to 0.9 fps (4x4). In the 2MHz digitization "speed mode," the camera increased from 1 fps to its maximal speed of 2 fps. Again, the SNR of the 2 MHz mode was higher than the 100 kHz mode for 1x1 binning. However, once the images began to be binned, SNR was approximately 10 for 2x2, 3x3, and 4x4 binning modes in both digitization modes.

2.4.1.3. Gain

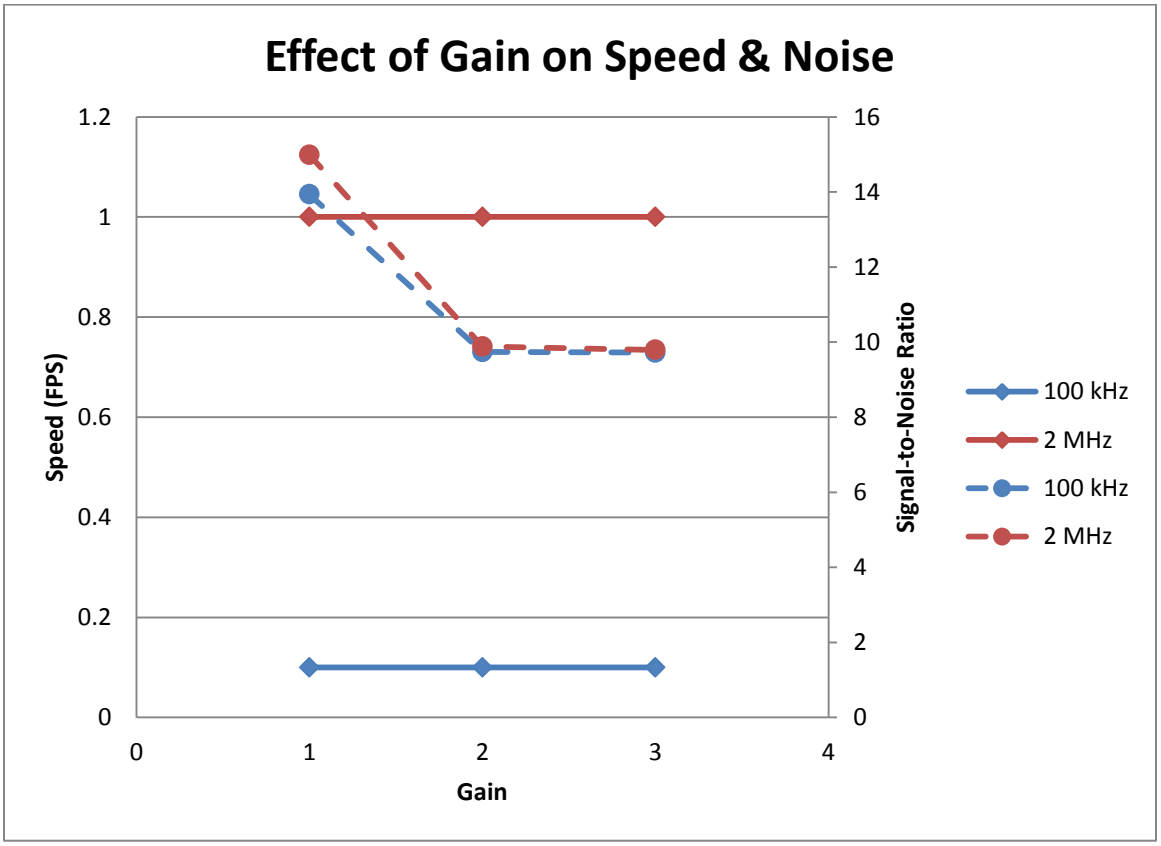

Figure 2.18 The change in speed and signal-to-noise ratio as a function of gain on the PIXIS 1024BR. Solid lines correspond to the left axis representing the speed of the detector, and dashed lines correspond to the right axis representing the signal-to-noise ratio.

Finally, in low light situations, the camera gain can be increased to amplify signals measured. Figure 2.18 shows the change in speed (solid lines) and SNR (dashed lines) as a function of image gain for each digitization mode of the PIXIS 1024BR. Since an increase in gain only amplifies the signal electronically, it has no effect on the speed of the camera in these tests, and therefore the speed remains constant as gain is varied. However, we see that as the gain is increased, the SNR for both digitization modes decreases. This is expected since amplifying electronic signals also introduces more noise into the signal. SNR drops significantly when the gain is changed from its default value of 1 to 2. However, there is only a very minor decrease for both digitization modes when changing from 2 to 3.

2.4.1.4. Conclusions

Overall, to produce high speed, quality images with the PIXIS 1024BR, these tests have shown that the 2 MHz digitization mode performs the same as, or sometimes better than the slower "low-noise" 100 kHz mode in terms of image SNR. Furthermore, the 2 MHz mode significantly outperforms the 100 kHz mode in imaging speed, ranging anywhere from double the frame rate to almost 10x the frame rate of the 100 kHz mode. Operating the camera at low exposure times, at its native gain of 1 and binning of 1x1, the camera exhibits the best SNR at an acceptable frame rate of 1 fps. Interestingly, when adjusting the binning and gain from their nominal values, the SNR of images drops significantly, but stays relatively constant, whether the user chooses a gain of 2 or 3, or binning of 2x2, 3x3, or 4x4. Therefore, in low light conditions, the user can feel confident adjusting the gain and binning within the aforementioned ranges, without further compromising image quality.

2.4.2. Spatial Resolution

Although image binning can significantly increase image capture rate, it also comes at the cost of decreased spatial resolution. To better understand the magnitude of lost spatial resolution, a quartz 1951 USAF resolution target was used as a standard to measure percent contrast versus

spatial resolution. The target was placed at a focal distance of 2 feet from the camera, and a broadband absorbance image was captured using a SRT-99-120 spectralon as a reflectance standard. Images were captured in 2 MHz digitization mode with a gain of 1, while the binning parameter was varied. Percent contrast for each line pair of the resolution target was calculated according to Equation 4

$$\%\ Contrast = \frac{I_{max} - I_{min}}{I_{max} + I_{min}} \cdot 100$$

Equation 4

where I_{max} is the maximum pixel intensity from a white bar, and I_{min} is the minimum pixel intensity from a black bar. Figure 2.19 shows the change in percent contrast as a function of spatial resolution for each of the four different binning modes of the PIXIS 1024BR.

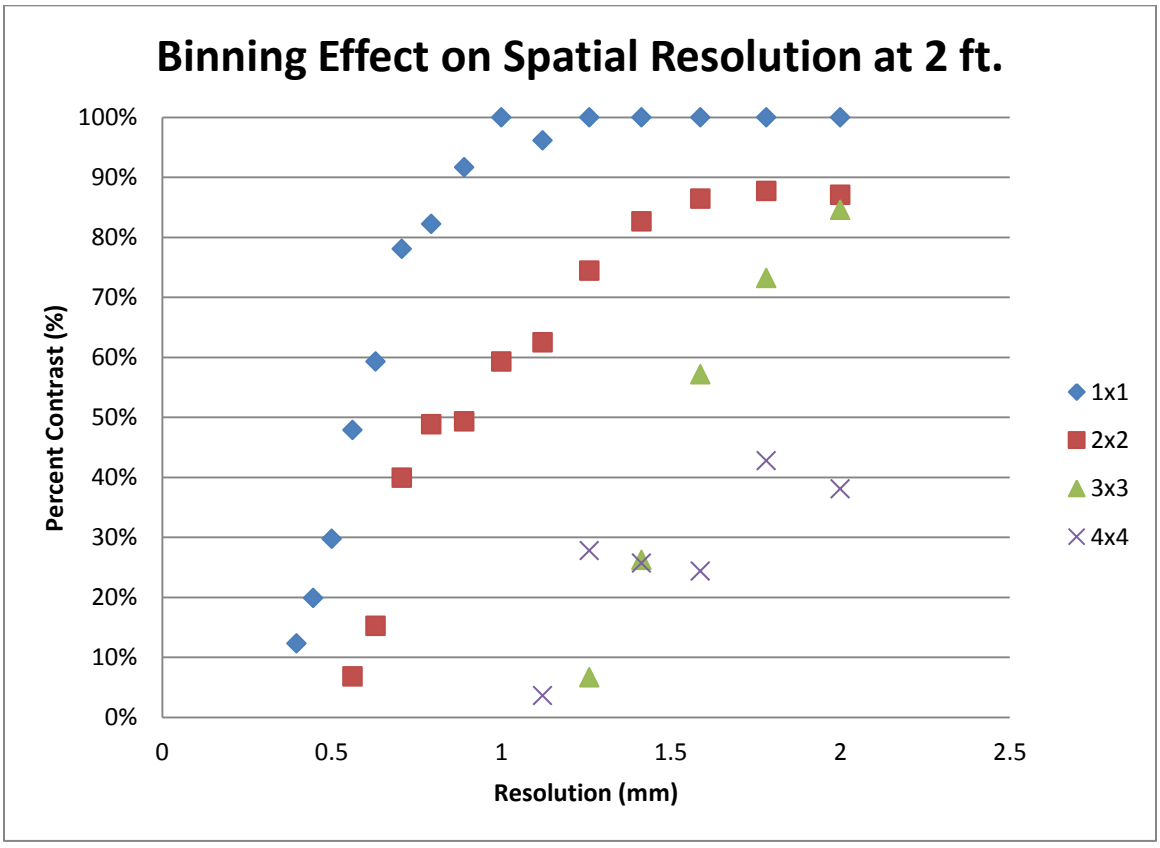

Figure 2.19 Change in percent contrast as a function of spatial resolution for each of the four binning parameters of the PIXIS 1024BR imaging the absorbance of a 1951 USAF resolution target from 2 ft.

As indicated by Figure 2.19, there are significant differences in the resolving capabilities of the PIXIS 1024BR depending on the user's choice of binning. In 1x1 mode, the user can obtain almost 0.5 mm of resolution with 50% contrast, whereas 4x4 binning cannot even attain 50% contrast at 2 mm of resolution from 2 feet away.

2.4.3. Conclusions

Overall, having a keen understanding of the detector's performance tradeoffs with different hardware settings can be extremely beneficial to the end-user and allows them to adapt the detector to different imaging environments. If the user is operating in conditions of low signal, and needs to keep the SNR low, varying the exposure time is the best way to gain more light without compromising noise. However, if the system needs to be faster and obtain more light, the user would have the choice of increasing the gain of the camera while decreasing exposure time, or bin images to get a significant boost in acquisition speed, but at the cost of spatial resolution. Overall, this characterization of the camera's speed, image noise, and resolution aid the user in understanding the limitations of the detector, and allow the user to choose hardware settings that are tailored to the demands of specific imaging applications.

2.5. Fluorescence Filter Transmission

Indocyanine green (ICG) is tricarbocyanine fluorescent dye that exhibits a typical Stoke's shift when it fluoresces light, meaning it emits light at higher wavelengths than it absorbs. The absorption spectra for ICG are depicted in Figure 2.20 and show that its absorption spectrum is dependent on solution-type as well as concentration of the fluorophore in the solution. Specifically, there is about a 25 nm shift in the absorption spectra when ICG is mixed in plasma versus water due to binding of the dye to plasma proteins. [20] In water, the apparent extinction coefficient has a maximum at λ = 695 nm with a shoulder at λ = 780 nm in high concentrations. As the solution is

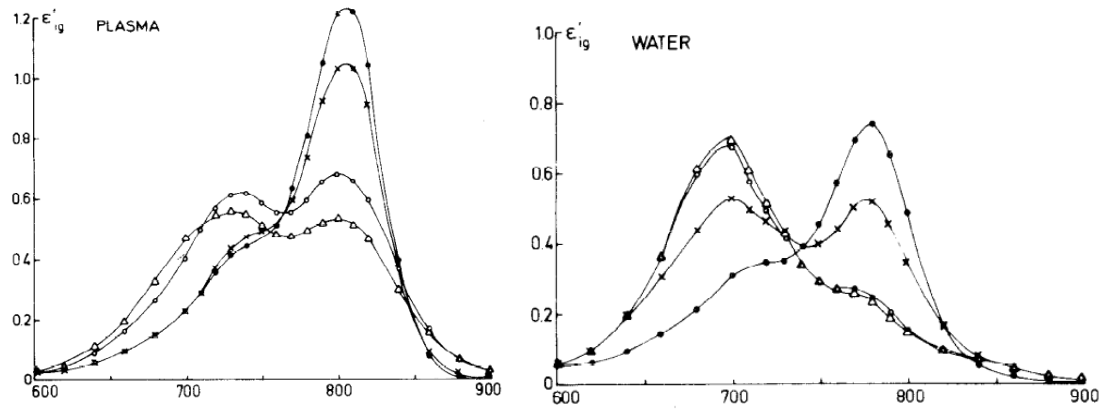

Figure 2.20 Absorption spectra of indocyanine green (ICG) in fresh pig plasma and water at concentrations of [Δ] = 1 mg/mL, [∘] = 0.5 mg/mL, [x] = 0.05 mg/mL, and [·] = 0.005 mg/mL.[20]

diluted from 1 mg/mL to 0.005 mg/mL, the spectra becomes bimodal before exhibiting a prominent peak at λ = 780 nm, and a shoulder at λ = 695 nm. Similarly, in plasma, ICG has two absorption maxima at λ = 730 nm and λ = 805 nm in high concentrations. However, as it is diluted in plasma, the maximum at λ = 805 nm increases dramatically, while the maximum at λ = 730 nm becomes more of a shoulder.[21] Furthermore, ICG fluoresces light at a maximum wavelength of λ = 820 nm in aqueous solutions and λ = 830 nm in human whole blood. The fluorescence intensity is also concentration dependent, exhibiting a maximum intensity at 0.08 mg/mL in human whole blood.[6]

Utilizing the capabilities of the OL490, the DLP® DMD chip will act as a filter for the excitation illumination of ICG, and will be discussed further in Chapter 3. Due to the shift of the absorption and emission spectra of ICG in different solutions, two different transmission filters were characterized to collect the fluoresced light while blocking the excitation illumination. An 805 Alpha Epsilon Long Pass (AELP) transmission filter (Omega Optical, Battleboro, VT) was used for lab experiments of ICG mixed in DI water, while an 815 Alpha Long Pass (ALP) transmission filter (Omega Optical, Battleboro, VT) was used for data collection in human surgery.

To characterize the transmission capabilities of the two filters, the USB 2000+ spectrometer, (characterized previously in Section 2.2.1) was coupled to a QP400-1-VIS/NIR fiber with a CC-3 cosine corrector (Ocean Optics, Dunedin, FL). The fiber with cosine corrector was placed a fixed

distance of 1 cm away from the output of the liquid light guide of the OL490 Agile Light Source. The OL490 was programmed to shine light with all mirrors in the 'on' position, and a spectrum was collected. Then each filter was placed individually in the light path between the source and detector without changing the source-detector distance, and a second spectrum was collected. Percent transmission was calculated by dividing the filtered spectrum by the unfiltered spectrum, and a plot for each filter's transmission as a function of wavelength can be seen in Figure 2.21.

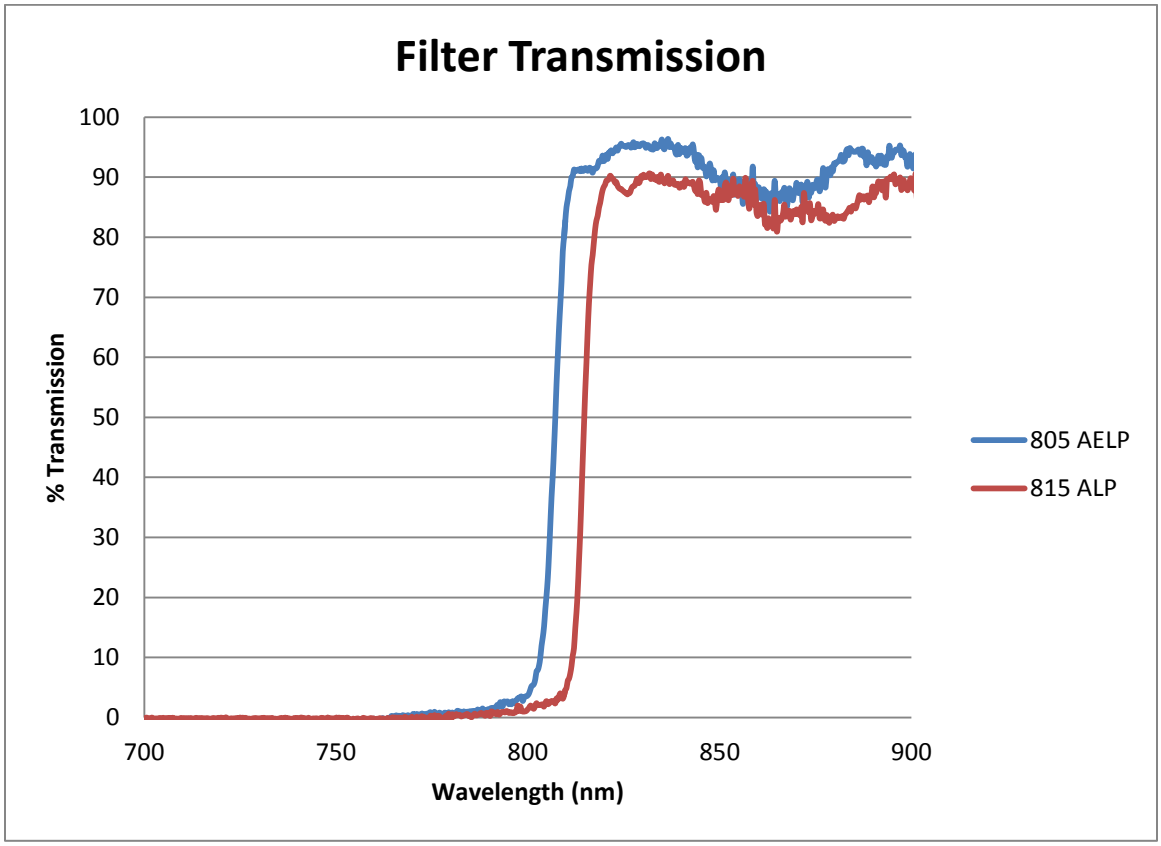

Figure 2.21 Transmission spectra of the 805 AELP and 815 ALP filters for ICG fluorescence detection

The 805 AELP filter exhibits 50% transmission at λ = 807.1 nm, 2.1 nm longer than the manufacturer's specification. However, since ICG is excited primarily at 780 nm and fluoresces primarily at 820 nm in water, this minor deviation should not have any significant effects. The 815 ALP filter exhibits 50% transmission at λ = 814.7 nm within less than 1 nm of difference from the ideal transmission cut-off.

2.6. White Matte Board

In hyperspectral reflectance imaging, a reflectance standard is required to calibrate the imaging system to account for spatial and spectral discrepancies with both the light source and detector. The standard is usually placed at the focal distance of the camera, and fills the field of view of the detector. Typically, a 12" x 12" SRT-99-120 spectralon is used as a reflectance standard because it could fill the field of view of previous hyperspectral imaging systems developed in this lab. [16, 24, 25, 26] However, the PIXIS 1024BR has a 18" x 18" field of view at a focal distance of 2 ft. so the SRT-99-120 would not allow for collection of accurate hyperspectral data in the periphery of the collected images.

Therefore, a larger 18" x 18" reflectance standard was sought out. However, the diffuse reflective material that spectralons are made out of is a low-density form of polytetrafluoroethylene (PTFE). Low density PTFE is relatively uncommon, and therefore not very cost-effective. Other studies have shown that more common materials with similar chemical compositions, such as high density PTFE, can be substituted as a diffuse reflectance standard. [27] Therefore, an 18" x 24" Ampersand Clayboard, commonly used by artists, was sourced and tested for its reflectance capabilities.

The 12" x 12" SRT-99-120 spectralon has a percent reflectance greater than or equal to 99% from λ = 350 nm – 1650 nm. Therefore, the white matte clayboard's reflectance was calibrated to that of the SRT-99-120 spectralon. The Mid-Range OL490 performed a 1 nm sweep over its entire spectral range, and the reflectance at each pixel of the CCD was compared to the spectralon target and averaged, with the resulting plot in Figure 2.22. Over wavelength range of the Mid-Range OL490, the matte clayboard has a relative % reflectance >85% compared to the spectralon standard, showing that it can reflect enough signal back to the detector to be used as a substitute reflectance standard in hyperspectral imaging applications. The clayboard's characteristic reflectance was normalized to that of the spectralon standard to obtain accurate hyperspectral images.

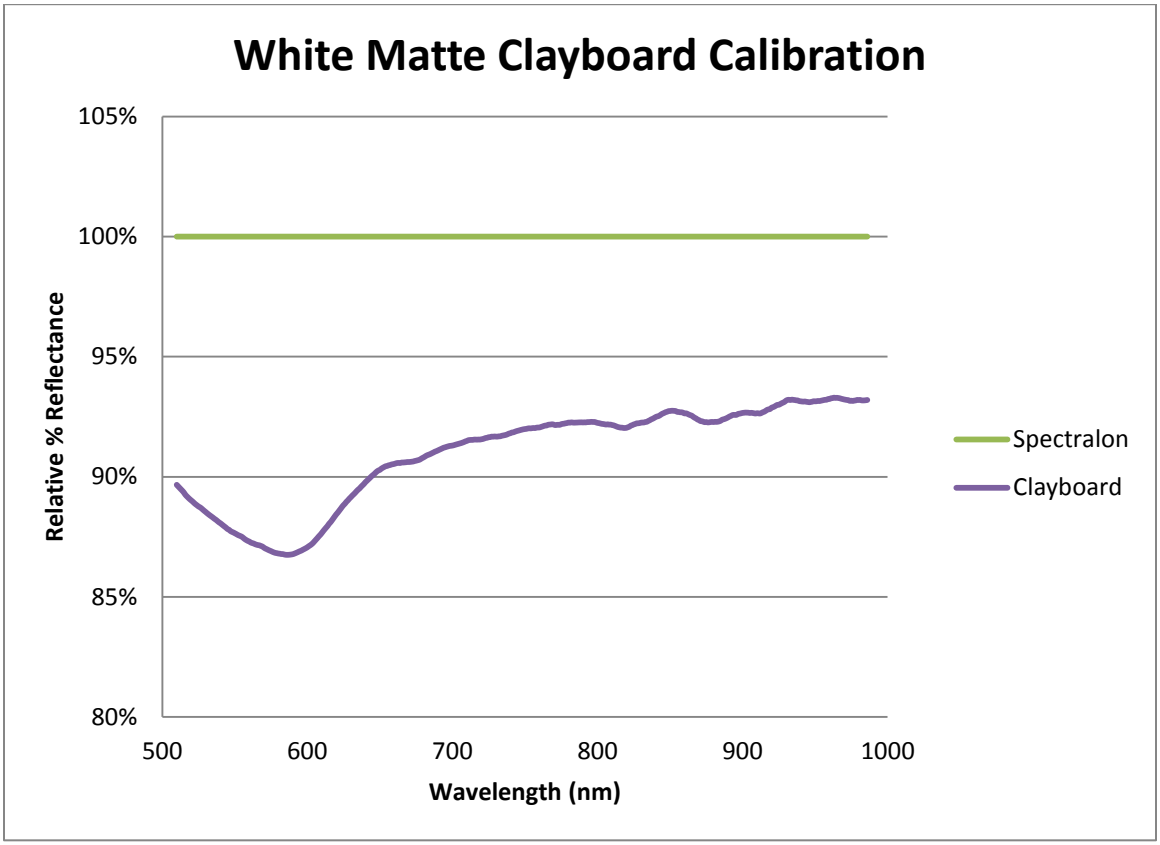

Figure 2.22 Relative % reflectance of an Ampersand Clayboard compared to a Labsphere SRT-99-120

CHAPTER 3

ILLUMINATION & IMAGE PROCESSING

Based on the characterization of the Mid-Range OL490 Agile Light Source, the dynamic source is capable of creating narrow or broadband spectra of continuous or non-continuous wavelengths with a spectral resolution of 1 nm, bandwidths as small as 8 nm, and 768 levels of intensity with up to 2,500 mW/cm^2 of power. The implementation of digital control over illumination spectra allows for this light source to execute different imaging applications and modalities with ease.

3.1. Oxy-Hemoglobin Absorbance

The Mid-Range OL490 was first adapted for hyperspectral imaging of oxy-hemoglobin (HbO_2) and deoxy-hemoglobin (Hb) which was originally based on liquid crystal tunable filter (LCTF) technology. [28] In 2009, the Laboratory of Biomedical Imaging at UTA began working with a visible wavelength OL490 (380 nm – 780 nm), which was then characterized to mimic the reflectance measurements of the LCTF-based system. Spectral measurements with this visible system have been successfully used in animal and clinical urological studies to create safer surgical practices in partial nephrectomy surgery. [17, 24, 25, 29, 30]

3.1.1. Hyperspectral Reflectance

The measurement of HbO_2 and Hb apparent absorbance using a Visible OL490 light source (380 nm – 780 nm) has been outlined in detail in a previous thesis by R. P. Francis. [15] Briefly, the OL490 is programmed to perform a λ = 520 – 645 nm x 1 nm contiguous sweep of wavelengths with approximately a 10 nm bandwidth. The camera-detector and light source are synchronized by a

laptop running software with a graphical user interface where the user can control parameters such as illumination mode, exposure time, binning, and camera gain. The sweep is performed on a diffuse, reflectance target (SRT-99-120) to obtain a calibrated "background" image, then, on a region of interest on biological tissue from the same distance.

A total apparent absorbance spectrum is derived for each pixel of the CCD from Equation 6

$$A_{xy}(\lambda_i) = \log_{10} \frac{R_{xy}(\lambda_i)_0}{R_{xy}(\lambda_i)_d}$$

Equation 5

where $A_{xy}(\lambda_i)$ is the apparent absorbance, $R_{xy}(\lambda_i)_0$ is the measured reflectance from the 99% reflectance target in units of counts, and $R_{xy}(\lambda_i)_d$ is the measured reflectance of the target of interest in units of counts for wavelength λ_i at spatial coordinates x and y. The total apparent absorbance spectrum is normalized and unmixed using a linear, least squares k-matrix method that assumes HbO_2 and Hb are the only spectra in the imaging scene. After unmixing, the relative contribution of the HbO_2 spectrum to the total apparent absorbance (the percent contribution) is saved at each pixel, color-coded, and written as an output image.

Based on the characterization of the Mid-Range OL490 system in chapter 2, the light source is capable of outputting light from 520 nm to 645 nm with a spectral bandwidth of 10 nm using the 350 μm slit. Furthermore, the imaging detector has a quantum efficiency above 60% over the wavelength range and is therefore capable of detecting changes in the absorbance of the protein hemoglobin.

3.1.2. 3-Shot Active Illumination

To make oxy-hemoglobin absorbance measurements more relevant for use in clinical surgery, the speed of chemically-encoded images was drastically increased by illuminating with a novel, patented, complex spectral illumination initially described in a thesis by R. P. Francis [15] and published by Zuzak et al.[16] Briefly, normalized reference spectra of HbO_2 and Hb are subtracted from

each other such that the positive remainder from HbO_2 – Hb is one complex illumination, and the positive remainder from Hb – HbO_2 is the other complex illumination. Essentially, these two complex illuminations are choosing the wavelengths of light that will highlight the differences in absorption between HbO_2 and Hb. Finally, a third illumination shines light over all wavelengths of interest and is divided by the difference of the first two illuminations to obtain a relative % HbO_2 value given in Equation 6 below

$$Relative\ \%\ HbO_2 = \frac{A_{HbO_2-Hb} - A_{Hb-HbO_2}}{A_{All}}$$

Equation 6

where $A_{HbO2\text{-}Hb}$ is the apparent absorbance of the positive remainder from HbO_2 – Hb spectra, $A_{Hb\text{-}HbO2}$ is the apparent absorbance of the positive remainder from Hb – HbO_2, and A_{All} is the apparent absorbance of all of the wavelengths evaluated over HbO_2 and Hb.

This method of illumination is significantly faster than the traditional bandpass hyperspectral imaging of HbO_2 and Hb for three major reasons. First, it involves simple mathematical calculations and does not involve spectral unmixing with significant matrix manipulation. Second, the use of complex spectral illumination means more light is exposed onto the target tissue for each image, reducing the exposure time required on the detector. Finally, the number of images is significantly reduced from 126 to 3, reducing the number of pixels to process from 132,120,576 to 3,145,728 pixels.

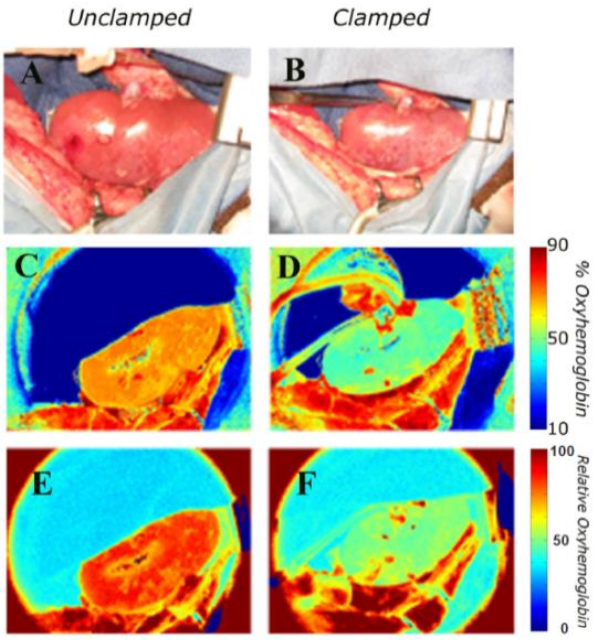

Figure 3.1 A comparison of the hyperspectral reflectance sweep to the 3-shot active illumination. Images of an unclamped and clamped (occluded) porcine kidney with digital (A & B), hyperspectral sweep (C & D), and 3-shot (E & F) chemically encoded images, respectively.[15]

A comparison of the 3-shot illumination and 126-shot spectral illumination can be seen in Figure 3.1, where both illuminations are measuring the relative contribution of HbO_2 absorption to the imaging scene. The spectral sweep method requires over 20 seconds to collect 126 images with the visible imaging system, and another 7.5 seconds to process the data, whereas the 3-shot method can capture images and produce a final, chemically-encoded image in 0.3 seconds, making it capable of seeing the dynamic changes in tissue oxygenation in real-time.

3.2. ICG Fluorescence

The Mid-Range OL490 was also adapted for fluorescence imaging of ICG, using the DMD as a customizable excitation filter for the fluorophore. As previously discussed in section 2.5, ICG has a different absorption spectrum depending on its containing solution. Therefore, optimizations in the excitation illumination of ICG fluorescence were first carried out in mixtures of DI water in the laboratory, with the understanding that the concepts learned could be translated to human clinical surgery once they were refined.

3.2.1. Tuning of Excitation Light

Although ICG is cited as having two wavelength peaks in water where maximal absorption of light occurs, the fluorophore will, in fact, absorb light over a large spectrum of wavelengths as seen in Figure 2.19. Therefore, instead of being selective with the excitation illumination, the goal is to excite with as much broadband light as possible without passing any light through the high-pass filter. The other goal of this excitation illumination tuning is to incorporate as much of the NIR wavelengths as possible to maximize the penetration depth of the illumination, since NIR wavelengths of light are known to penetrate deeper into biological tissues. [31]

Previous work in the Laboratory for Biomedical Imaging at UTA, characterized the absorption spectra for ICG, and found that solutions of ICG greater than 0.015 mg/mL formed aggregates in solution and greatly affected the absorption spectra. [32] Therefore, for these laboratory experiments, 0.6 mg of Cardiogreen (Sigma-Aldrich, St. Louis, MO) was mixed with 40 mL of deionized (DI) water to create a 0.015 mg/mL solution of ICG. Two capillary tubes were placed at a focal distance of two feet from the detector and light source, one filled with the ICG mixture, and the other with DI water. The 805 AELP long pass filter was mounted on the detector's lens to block excitation light below 805 nm, but to let fluorescent light pass above 805 nm.

Previous work by Mangum et. al., identified a method of creating increasing short-pass filters with the OL490 to identify the optimal excitation wavelengths of light for ICG fluorescence. [33] Briefly, all wavelengths of light below 775 nm were illuminated at full intensity, and the upper "filter" cutoff of the excitation light was increased at 5 nm increments from 775 nm to 810 nm, to determine the region where ICG fluorescence was maximized. Figure 3.2 depicts this illumination scheme showing where each illumination intersects the transmission of the long pass filter. As the upper "filter" cutoff is slowly increased, more and more of the excitation illumination passes through to the detector and washes out the ICG capillary tube as seen in Figure 3.3.

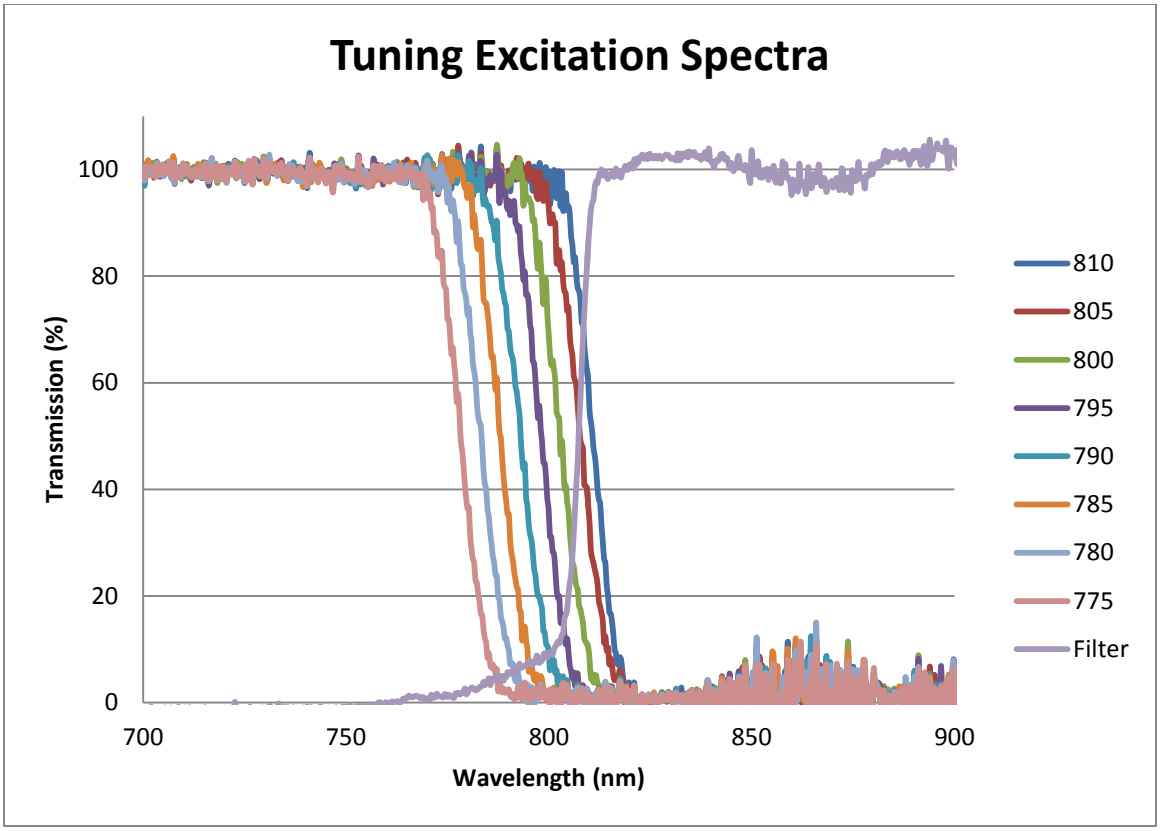

Figure 3.2 Tuning of the excitation illumination for ICG fluorescence.

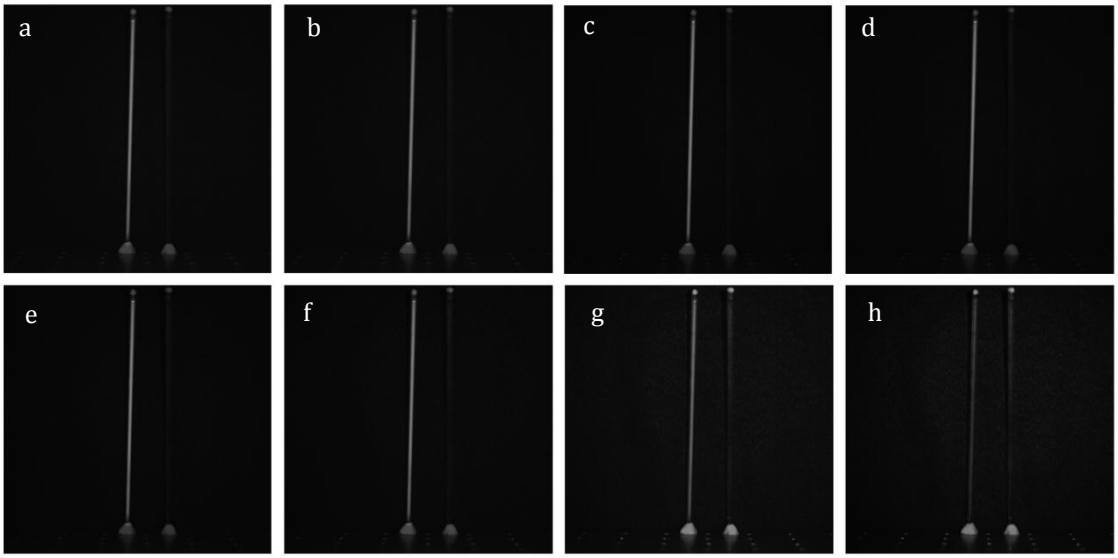

Figure 3.3 The change in ICG fluorescence as the excitation illumination slowly spills over into the detector of the imaging system. Spectral cut-offs of (a) 775 nm, (b), 780 nm, (c) 785 nm, (d) 790 nm, (e) 795 nm, (f) 800 nm, (g) 805 nm, and (h) 810 nm.

Capillary tubes were imaged in a black box inside the lab, with the understanding that this would be the ideal conditions for ICG fluorescence. Two different methods for image processing were also considered during this analysis. The first was simply to acquire raw images, and the second process was to take a dark background without the capillary tubes in the field of view, to subtract from the raw picture.

To quantitatively determine the best excitation illumination, percent contrast of the fluorescent capillary tube was measured with respect to the DI water capillary tube for both the raw (Data) images and the dark-subtracted images (Data Minus Dark). The raw data images show an impressive percent contrast above 80% up to 800 nm of light, however, beyond 800 nm the contrast quickly drops off, and this is visually evidenced by examining Figure 3.3 (g) and (h), where in (g), you can begin to see the DI water capillary tube, and by (h), the two capillary tubes are indistinguishable from one another.

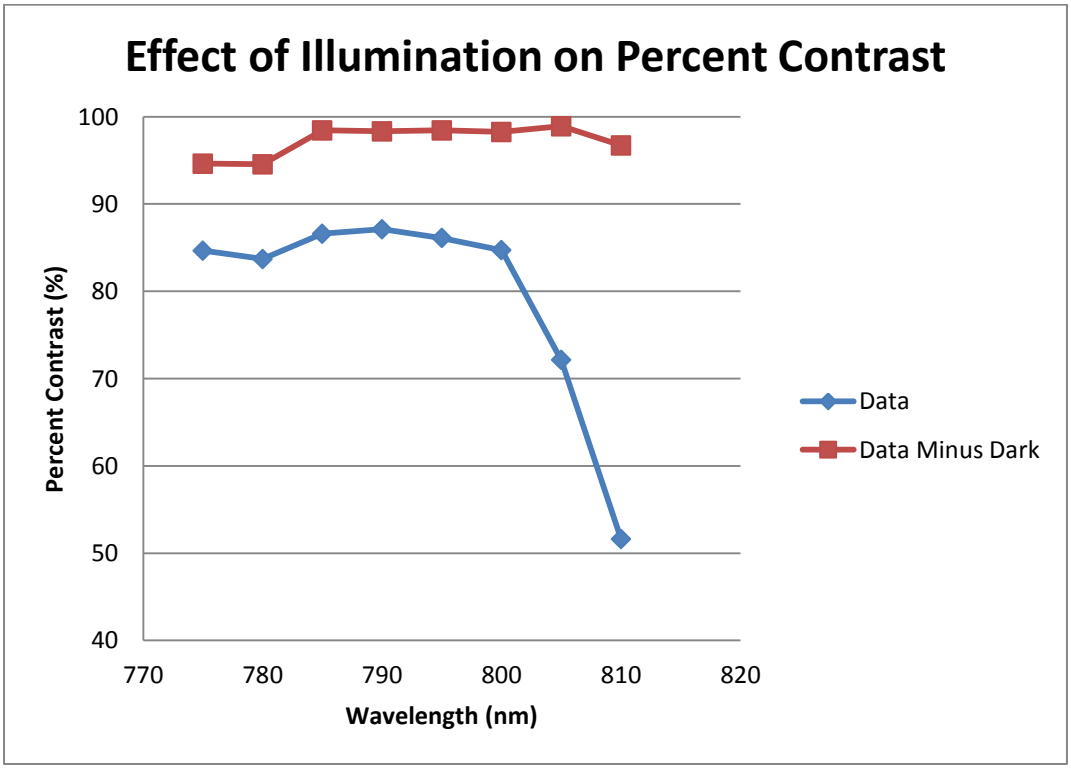

Figure 3.4 Change in percent contrast of ICG fluorescence as a function of short pass filter cutoff wavelength. [33]

Based on Figure 3.4 above, it was interesting to see both image processing modes gaining a significant increase in percent contrast after 780 nm, one of the absorption maxima for ICG in water. Furthermore, the best percent contrast of raw 'Data' images fell in the range of cutoffs from 790 nm to 795 nm. Therefore, mirror columns were stepped one at a time over this range, and it was determined that the excitation illumination with the highest percent contrast was mirror column 531, with a center wavelength of 794.0 nm and bandwidth of 12.6 nm, corresponding to a percent contrast of 87.2% for raw 'Data' images and 99.1% for 'Data Minus Dark' images.

3.2.2. Spot Diameter

In an effort to further optimize the fluorescence of ICG, the adjustable beam-shaping optic was implemented to control the spot size of the excitation illumination on the fluorescence target. Again, two capillary tubes, one of DI water and one of a 0.015 mg/mL solution of ICG were imaged at a distance of 2 feet from the detector and light source. The tubes were illuminated with the ideal excitation spectrum discussed previously, while the spot size of the optic was adjusted to the following diameters on the imaging target: 1.75", 6", 12", 18", and 26". Figure 3.5 shows the change in percent contrast for both fluorescence image processing modes.

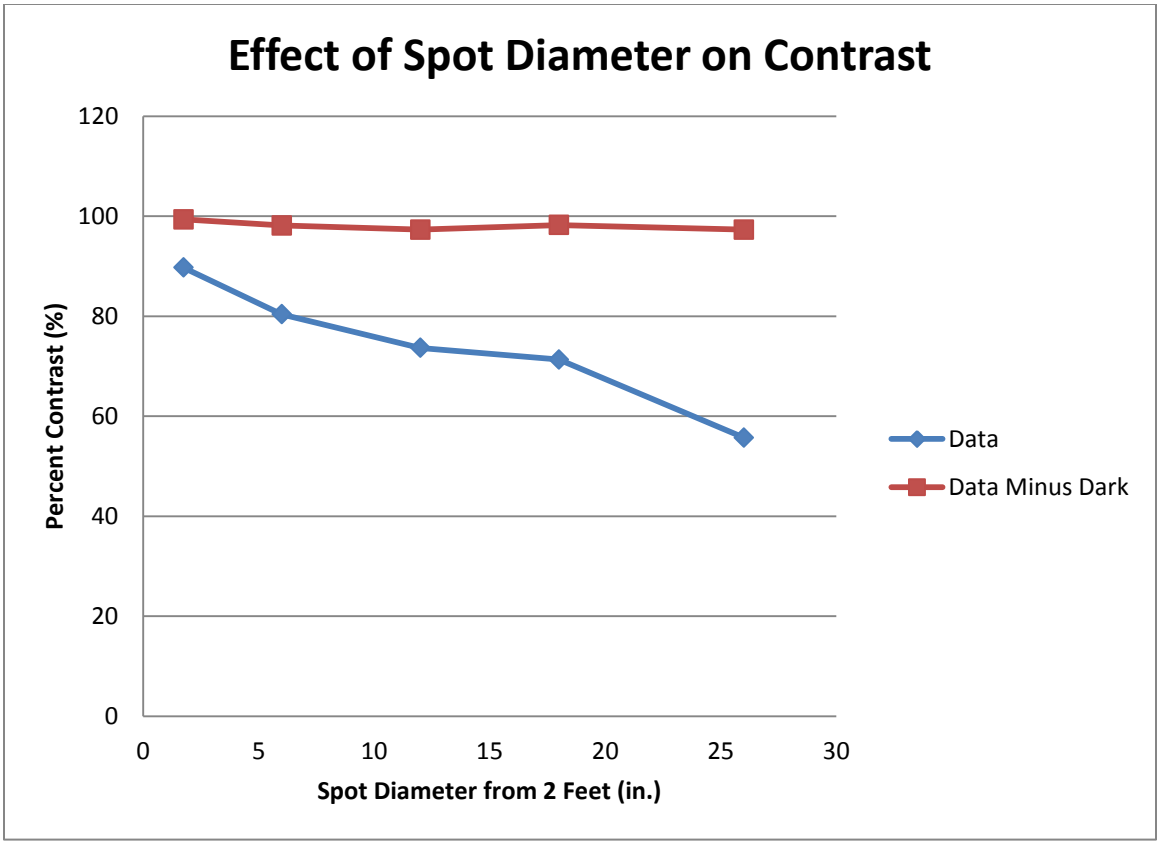

Figure 3.5 The effect of changing the spot diameter on the imaging target on percent contrast. [33]

As expected, when the spot size of the illumination increases, the excitation light becomes more diffuse, which decreases the efficiency of fluorescence. However, by subtracting dark counts of the same illumination, there is almost no change in percent contrast, and the percent contrast of the resulting images stays above 97% for all spot diameter sizes. Therefore, for future imaging of ICG fluorescence, the adjustable illumination optic's spot diameter should be minimized as much as possible to concentrate the excitation illumination as much as possible to obtain maximal contrast between ICG and the background.

3.3. Safety of Illumination

Prior to implementation of both the hyperspectral and fluorescence imaging modalities *in vivo*, the safety of the chosen illumination spectra should be investigated. The International Electrotechnical Commission specifies a thermal hazard exposure limit for skin over the visible and

infrared wavelength range (380 nm to 3000 nm). [34] The specification states that radiant exposure of the skin should be limited to

$$E_H \cdot t = \sum_{380}^{3000} \sum_{t} E_\lambda(\lambda, t) \cdot \Delta t \cdot \Delta\lambda \leq 20{,}000 \cdot t^{0.25}$$

Equation 7

where $E_\lambda(\lambda,t)$ is the spectral irradiance in units of watts per meters squared per nanometer ($W/m^2 \cdot nm$), $\Delta\lambda$ is the bandwidth of the illumination in units of nanometers (nm), and t is the exposure time in units of seconds, and must be less than 10 seconds. The authors state that this limit is based on thermal skin injury due to small area irradiation. Furthermore, large area irradiation limits cannot be specified because this requires consideration of the heat exchange between the individual and their environment. [34] Although the article does not explicitly state the sizes of a "small" and "large" area, it is still good to understand if there are any risks to using the chosen illuminations prior to their use.

All *in vivo* imaging will take place at a minimum distance of 2 feet from the biological tissue target. Therefore, knowing the irradiance of the light exiting the 3 mm LLG of the OL490 at every wavelength, and that irradiance decreases with the square of distance, we can calculate a conversion factor between the irradiance at the end of the LLG of the OL490 and the irradiance at the biological tissue surface two feet away.

$$E_{LLG}(\lambda, t) \cdot A_{LLG} = E_{target}(\lambda, t) \cdot A_{distance}$$

$$E_{target}(\lambda, t) = E_{LLG}(\lambda, t) \cdot \frac{\pi\left({}^{0.003}/_{2}\right)^2}{4\pi\left(2\ ft \cdot \frac{0.3048\ m}{1\ ft}\right)^2} = E_{LLG}(\lambda, t) \cdot 1.51e^{-6}$$

There are three major illuminations that will be used by the Mid-Range OL490 imaging system: (1) A hyperspectral bandpass sweep from 520 nm to 645 nm at a bandwidth of 13 nm for the 350 μm slit, where typically, each bandpass has a 100 ms exposure time, (2) the 3-Shot active

illumination which has a variable exposure time of approximately 1 second, 0.5 seconds, and 0.25 seconds for the first, second, and third frames, respectively, and (3) the fluorescence excitation illumination which is a broadband, 100% illumination from the lower limit of the OL490 around 504 nm to 794 nm.

For the traditional 126-shot bandpass method with a constant exposure time of 100 ms for each frame, the safety limit equals 25,396.5 J/m^2. Choosing the most powerful bandpass of the 126 shots that will be exposed on the patient, the irradiance at the LLG is 8,915.5 W/m^2, but the irradiance at the surface of the patient is 0.0135 W/m^2. Every other bandpass illuminated from the OL490 will be less powerful than this bandpass, so using the most powerful bandpass for all 126 shots, the biological tissue will feel a total irradiance of 1.7 J/m^2 over 12.6 seconds, guaranteeing that the 126-shot bandpass method will be safe for use *in vivo*.

For the 3-shot active illumination, with a variable exposure time of approximately 1 second for the first shot, 0.5 seconds for the second, and 0.25 seconds for the 3rd, the safety limit equals 23,003.3 J/m^2. After calculating Equation 7 for the 3-shot active illumination, the total power density is 0.05 J/m^2.

Finally, for the excitation illumination of ICG fluorescence, exposure times could reach a maximum of 2 seconds depending on lighting conditions, since fluorescence involves the generation of photons from the ICG solution, and ICG has a quantum yield of 0.0028 in water and 0.012 in whole blood. [6] Therefore, the thermal hazard exposure limit for skin is 23,784.1 J/m^2. However, the excitation illumination will only reach a power density of 470.7 J/m^2 in practical use.

CHAPTER 4

CLINICAL STUDIES

4.1. Ethical Considerations

Prior to any collection of *in vivo* imaging data, a protocol was submitted and accepted by the Institutional Review Board at UT Southwestern Medical Center (Study ID: STU 082010-299). Patients were informed in detail of the risks of imaging, and consent was received prior to commencement of any imaging in the surgical operating room.

4.2. Breast Reconstruction Surgery

4.2.1. Overview & Surgical Problem

In 2010, over 93,000 breast cancer patients elected to have breast reconstructive procedures after undergoing either lumpectomy or mastectomy. [35] Typically, after cancerous tissue has been removed from the chest wall, autologous skin flaps from the abdomen are used to reconstruct the missing breast mound as depicted in Figure 4.1.

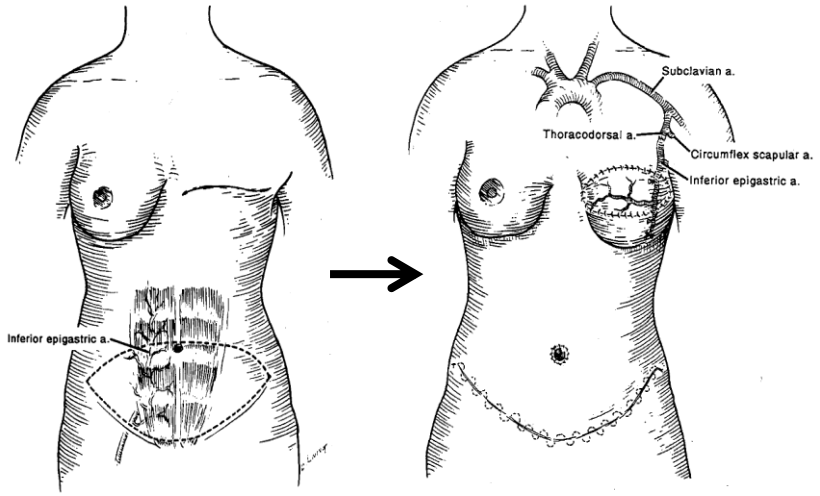

Figure 4.1 Basic steps in abdominal flap-based breast reconstruction.[36]

When the skin and fat tissue is harvested and transferred up to the chest wall, the surgeon must anastomose (join end-to-end) a perforating artery and vein from the flap to the thoracodorsal artery and vein, respectively, as seen in Figure 4.1. This anastomosis will provide oxygenated blood and nutrients to the transferred flap. However, if too much skin and fat tissue is transferred to the breast without adequate blood perfusion, the flap will begin to die, and a second revision surgery will be required to remove any necrotic tissue.

Typically, for a patient with no previous history of abdominal surgery, there will be multiple perforators for the plastic surgeon to choose from to use in the flap harvest. However, surgeons do not have many tools at their disposal to determine the vascular territory, or perforasome, of a particular perforator artery that they've chosen to use. In fact, beyond locating the perforator with Doppler detection and physically examining the size of the perforator, the surgeon has to use their clinical judgment based on previous experiences to determine how large of a flap they can harvest.

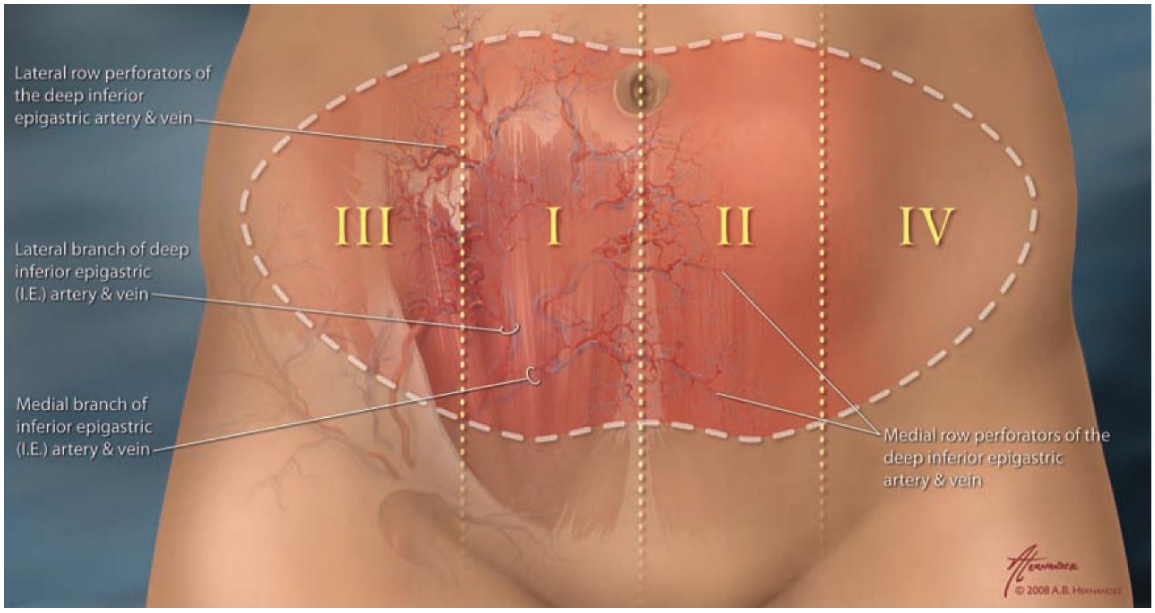

Figure 4.2 The zones of perfusion of a Deep Inferior Epigastric Perforator (DIEP) flap used in breast reconstruction.[37]

Therefore, a lot of free flap literature has focused on statistically determining where the largest perforators will be located, and identifying zones of perfusion where certain regions of the flap are more likely to survive harvest and avoid fat necrosis.[37, 38] Furthermore, contrast computed tomography (CT) imaging has been used in cadavers to begin to better understand the vascular territories of different perforators in both pedicled and free flaps.[39] Incidentally, it has been determined that the perforasome of a single perforator can be greatly extended beyond its normal physiological size, if there is exceptional flow shunted toward this perforator.[40] Figure 4.3 illustrates this idea, where a single harvested perforator at the top of the image normally only supplies a circumferential area of skin and fat tissue directly surrounding the central perforator. However, if there is increased flow in the perforator, direct and indirect linking vessels can also receive fresh oxygenated blood, thus extending the vascular territory, or perforasome, of the flap.

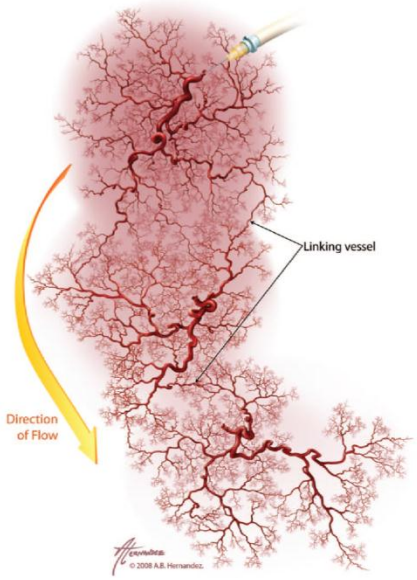

Figure 4.3 Increase in the perforasome of a single cannulated perforator due to direct and indirect vessel linking. [40]

Ultimately, plastic surgeons want to know if the skin flap they're transferring to the patient's chest wall is going to survive without partial flap necrosis or total flap loss due to venous occlusion. Therefore, the Mid-Range DLP® imaging system was employed to measure the spatial distribution of relative % of oxy-hemoglobin in patient's skin flaps which are undergoing Deep Inferior Epigastric Perforator (DIEP) flap breast reconstruction surgery in an effort to reduce the occurrence of fat necrosis or venuous occlusion in these flaps.

4.2.2. Methods

The Deep Inferior Epigastric Perforator (DIEP) flap breast reconstruction was used as the clinical model to attempt to detect changes in tissue oxygenation in abdominal skin flaps used in breast reconstruction. Prior to collecting clinical data, the surgeon had some requirements for the system. It must be able to acquire chemically-encoded images without movement artifacts, have a field of view large enough to contain the entire flap of 2 ft. from a 2 ft. distance, and it must produce high resolution images.

Based on previous characterization of the Mid-Range system in Chapter 2, the light source behaves similarly to the Visible OL490 system, and original LCTF technology when using the 350 μm slit. Based on characterizations of the camera, its' fastest image acquisition speed is 2 fps, meaning one would obtain two chemically-encoded images every 3 seconds. Considering patients can take up to 12 breaths per minute (1 breath every 5 seconds) under anesthesia, the camera simply cannot operate quickly enough to satisfy the Nyquist criterion of 2 samples per cycle. Therefore, instead of tailoring the hardware for speed, it was tailored for high resolution images at longer exposure times, which required holding the patient's breathing during imaging, which lasted approximately 1 second.

During clinical surgery, prior to imaging, the lamp was always allowed to warm up for 20 minutes to come to a steady state temperature and operation. A Leica DISTOD2 laser distance finder was used to remotely measure the distance between the optical equipment and the reflectance standard as well as the patient. The white clayboard, characterized as a reflectance standard, was used to calibrate the imaging system and fill the entire field of view of the detector. The imaging system was calibrated to the white clayboard standard at a distance of 2 ft. Counts measured by the detector for each of the 3 shots were maximized to 60,000 counts, just below saturation of the camera, so that any specular reflection from the images would result in saturated pixels that would not be used in image analysis. To date, 7 DIEP flap patients have been imaged with the 3-shot active illumination to determine their relative % HbO_2 levels at various time points in breast reconstruction surgery.

4.2.2.1. Mapping perforasomes

The perforasome of the perforator selected by the plastic surgeon was evaluated with hyperspectral imaging prior to the flap being transferred, so the surgeon would better understand the margins of healthy tissue. During the DIEP flap surgery, the physician removes all underlying vasculature to the skin and fat tissue except for the single perforator that will be used to oxygenate the flap once transferred to the chest wall. When the flap is in this condition, it is considered

"dissected." After complete dissection, the entire candidate, dissected flap was flattened by placing towels under the lateral edges, and imaged using the 3-shot method while the patient's breathing was temporarily held.

4.2.2.2. Perforator selection

To aid plastic surgeons in choosing the best perforator, all vasculature was removed from patient's abdominal skin flap, except for candidate perforators with a diameter of 3 mm or larger. Perforators were selectively occluded using temporary clips, and changes in tissue oxygenation were observed with 3-shot hyperspectral imaging. Once perfusion to the flap had been changed for approximately 5 minutes, the patient's breathing was held temporarily while a 3-shot hyperspectral image was collected.

4.2.2.3. Flap Monitoring Over Time

Finally, skin flaps were imaged over the duration of the surgery to monitor changes in tissue oxygenation levels. Because this is a free flap surgery, the flap will be completely cut-off from the patient's blood supply, making it completely ischemic, while the surgeons work to anastomose the artery and veins to the chest wall. After the anastomosis is complete, blood flow is restored to the flap and it is reperfused. Skin flaps were monitored prior to ischemia, during ischemia, and after the flap was reperfused to see the extent of the changes in tissue oxygenation. The surface of the flap was flattened prior to each imaging session, and if the flap was attached to the patient's body, breathing was held temporarily to avoid movement artifacts.

4.2.3. Results & Discussion

4.2.3.1. Perforasome Mapping

3-shot hyperspectral images of the dissected skin flaps were successfully collected and analyzed using MATLAB software (Mathworks, Natick, MA). The resulting image, displayed in Figure

4.4, is of a flap that was dissected and had a single medial perforator on the left side providing oxygen to the entire flap. The image is color-coded to show relative percent oxy-hemoglobin (% HbO_2) over the surface of the flap.

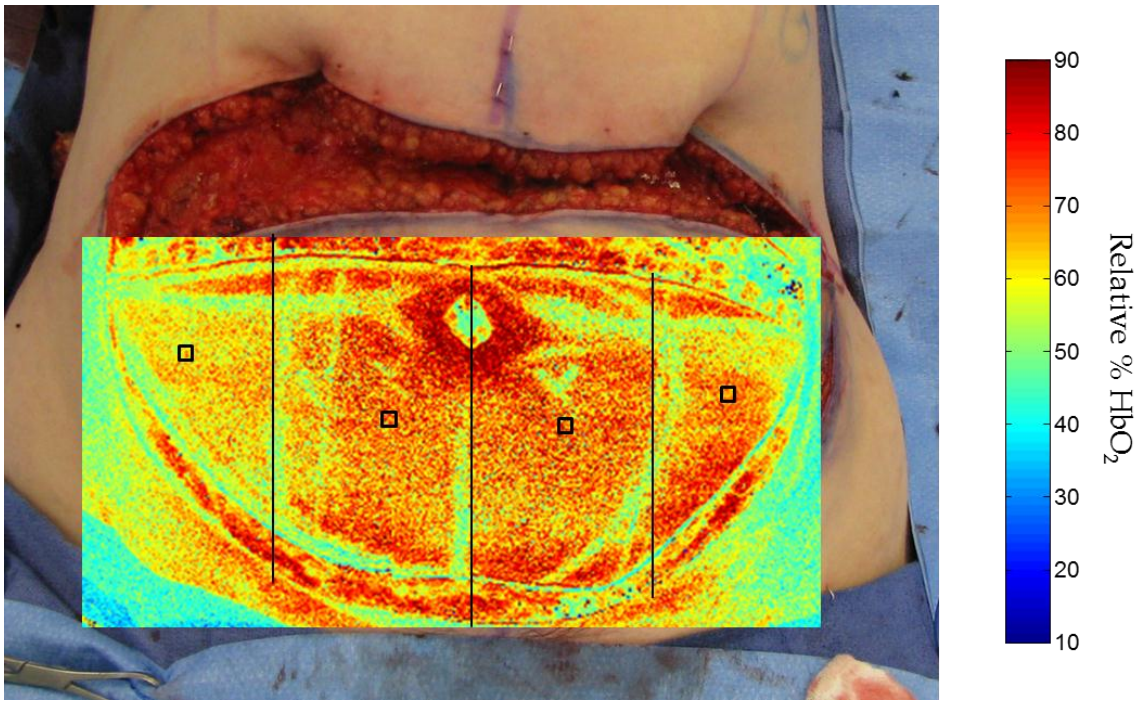

Figure 4.4 Example 3-shot hyperspectral image of a dissected skin flap during DIEP flap breast reconstruction surgery.

Image analysis was performed by selecting boxes of pixels, as seen in Figure 4.5, and averaging the values inside. The resulting averages for each of the four flap zones, along with their standard deviations are shown in Figure 4.4.

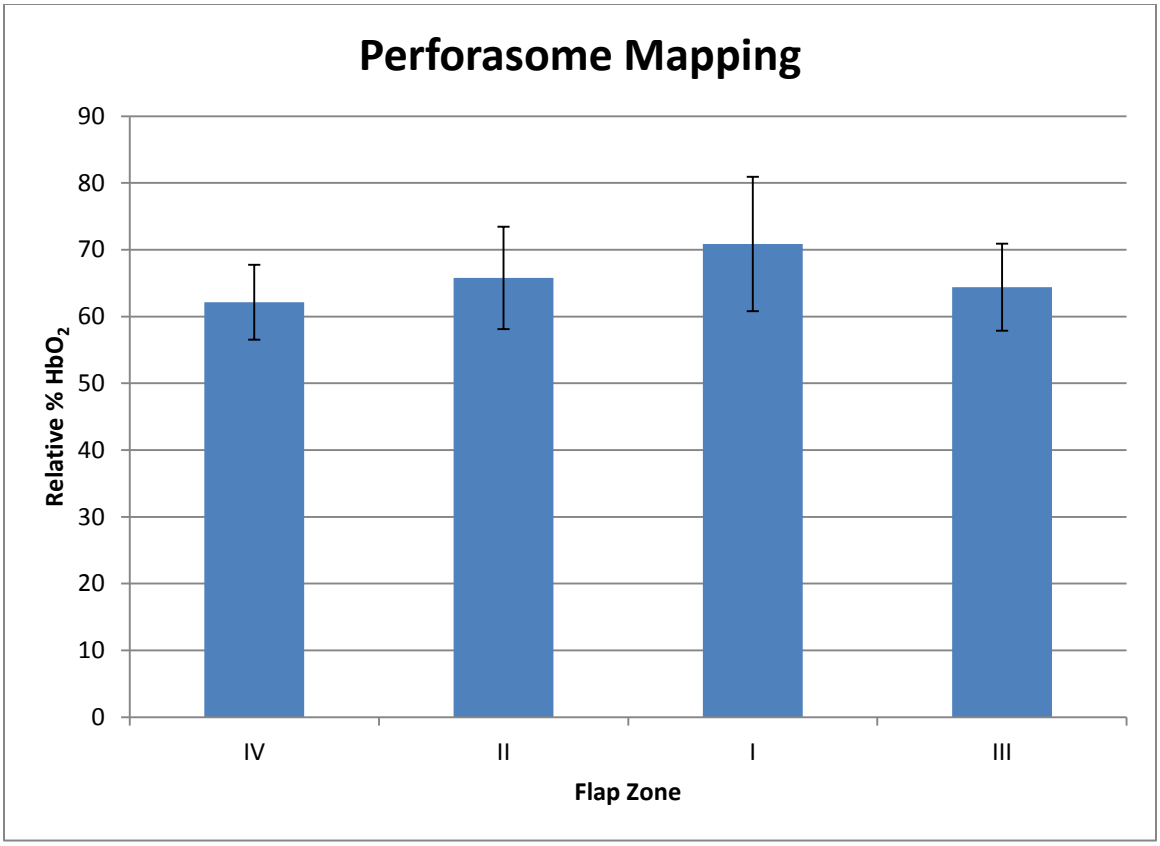

Figure 4.5 The average relative % HbO_2 of the boxes in each of the four flap zones of Figure 4.4.

The relative % HbO_2 values for each of the four zones of the flap were 70.9%, 65.8%, 64.4%, and 62.2% for zones I, II, III, and IV, respectively. This coincides with theoretical models which say that zone I of the flap, where the major perforator is located, should be the best perfused, and zone IV, contralateral to the perforator should be the least perfused.[37] Two-sample, two-tailed Student's *t*-tests assuming unequal variances were performed, comparing flap zones I & II, II & III, and III & IV. All tested groups were determined to have statistically significantly different mean tissue oxygenation values, with *p*-values less than 0.05. 3-shot hyperspectral images for this patient's dissected flap independently confirmed the surgeon's intuition to leave out Zone IV from the breast reconstruction, as seen in Figure 4.6. The patient's breast reconstruction post-op resulted in no complications due to partial flap necrosis.

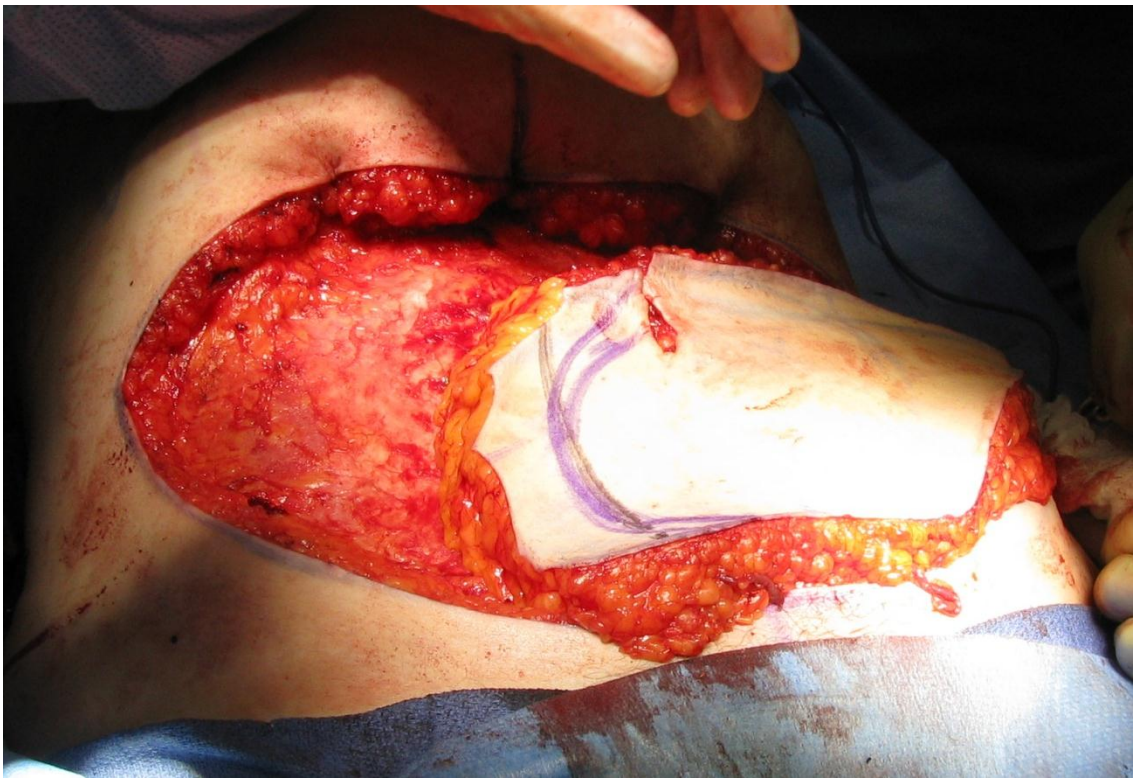

Figure 4.6 Flap harvested by the plastic surgeon, showing that the surgeon chose to use Zones I, II, and III of the flap, but discarded Zone IV to avoid partial flap necrosis.

4.2.3.2. Perforator Selection

Selective clamping of flap perforators was also employed to evaluate changes in the vascularization of skin flaps, and to potentially identify the perforasomes of individual perforators. The skin flap imaged in Figure 4.7 has three physiologic perforators: one lateral perforator with a 3 mm diameter, and two medial perforators with diameters of 4 mm and 5 mm. The lateral perforator was clamped for approximately 4 minutes, then the flap was re-imaged to visualize any changes in tissue oxygenation, specifically in the lateral aspects of the skin flap. The same analysis procedure was used as in section 4.2.3.1, where pixels in a selected square area were averaged in each image, and resulted in tissue oxygenation values of 59.7% and 59.6% for the unclamped and clamped conditions, respectively. Two-sample, two-tailed Student's *t*-tests assuming unequal variance showed no statistically significant difference between the two conditions.

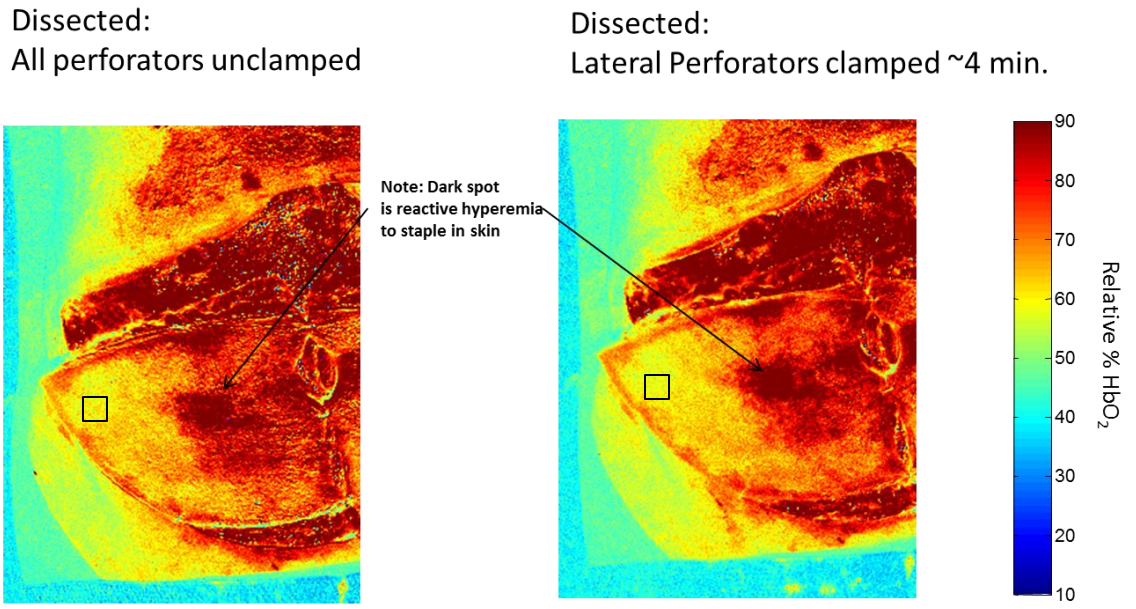

Figure 4.7 3-shot hyperspectral images of a dissected skin flap, where all perforators are perfusing the flap (left), and only medial perforators are perfusing the flap (right)

The lack of change in $\%HbO_2$ between the two conditions is initially counterintuitive. However, it can be attributed to compensatory flow from the neighboring medial perforators due to decreased resistance from the competing flow of the lateral perforator, as well as the release of vasodilators and other vascular factors in the lateral region encouraging increased blood flow.

4.2.3.3. Flap Monitoring Over Time

Relative % HbO_2 values were measured over the course of the reconstruction surgery, near the flap's perforator and at the lateral edge of the flap where tissue necrosis is most likely to occur. Figure 4.8 shows a series of 3-shot hyperspectral images beginning with a fully-dissected flap (a), the flap after it has been ischemic for 14 minutes (b) and 75 minutes (c), and the flap after it has been re-perfusing on the chest wall for 11 minutes (d) and 114 minutes (e). Again, a square area of pixels was selected next to the flap's perforator and near the lateral edge of the flap. The pixels were averaged and plotted in Figure 4.9 to see the changes in tissue oxygenation over time.

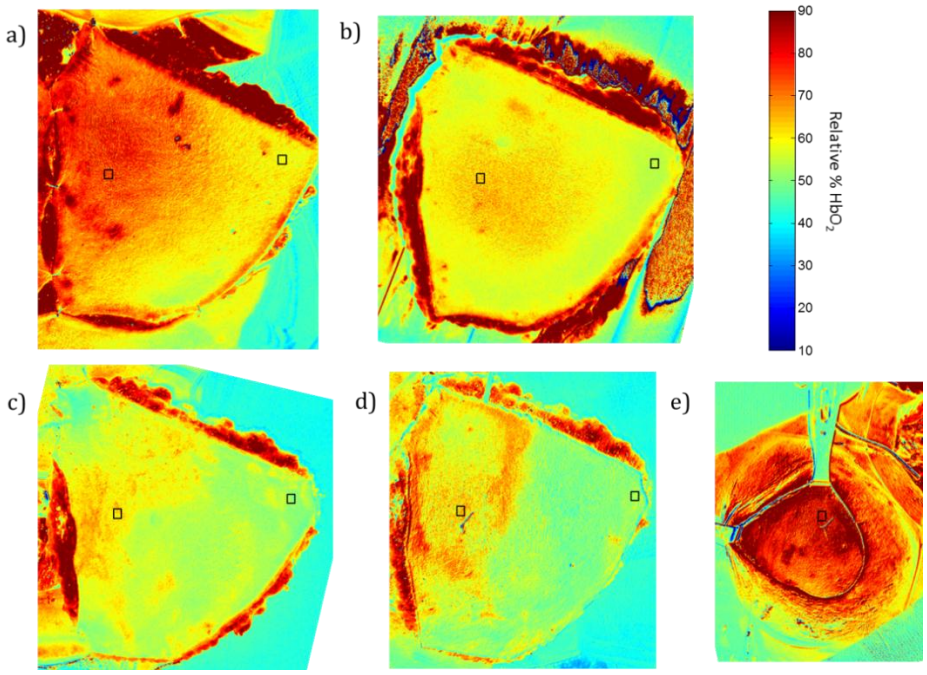

Figure 4.8 3-shot hyperspectral images of the skin flap over time, beginning with the flap fully dissected on a single perforator (a), the flap after it has been ischemic for 14 min. (b) and 75 min. (c), and the flap after it has been re-perfusing on the chest wall for 11 min. (d) and 114 min. (e). The black squares indicate analyzed regions of the flap next to the perforator and at the lateral edge of the flap where necrosis is most likely to occur.

The changes in $\%HbO_2$ over time decreased during ischemic time and increased during re-perfusion of the flap as expected. Furthermore, for this particular patient, the re-perfused flap on the chest wall showed to have higher relative $\%HbO_2$ values than the dissected flap sitting on the abdominal wall (80.5% vs. 75.2%, respectively), suggesting that the flap was being hyperperfused due to increased blood flow from the thoracodorsal vasculature of the chest wall.

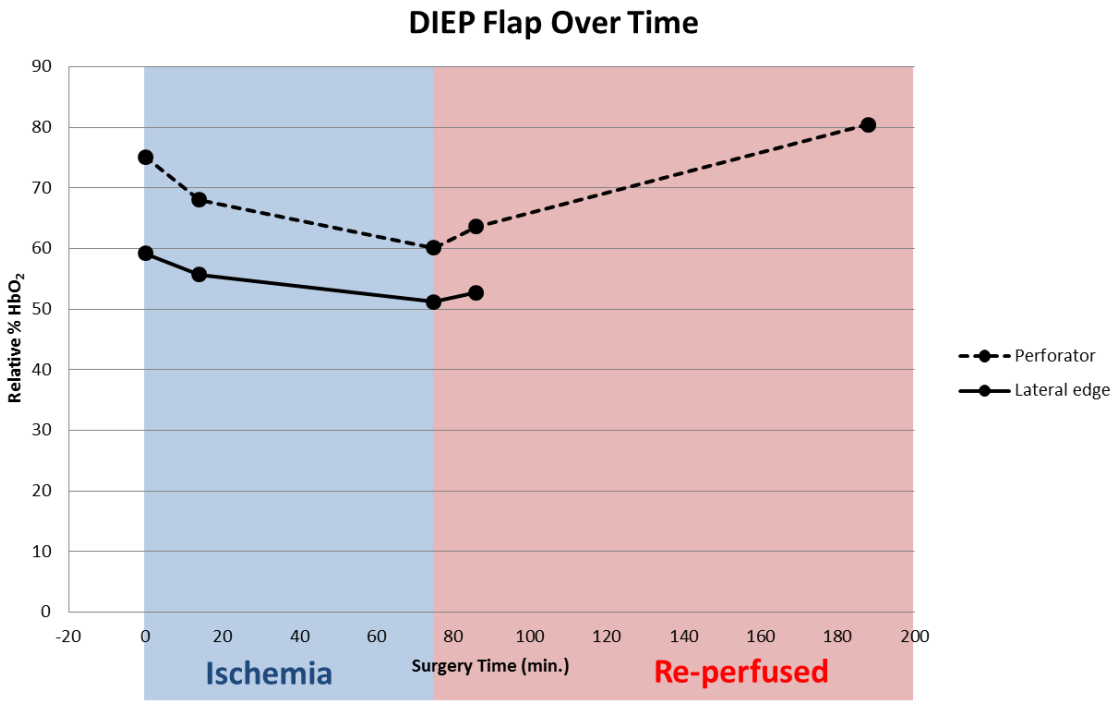

Figure 4.9 Changes in relative % HbO_2 at the perforator and lateral edge of a DIEP free skin flap over time.

4.2.4. Conclusions & Future Work

Overall, 3-shot hyperspectral imaging is a relatively fast and sensitive method to detect changes in tissue oxygenation of free skin flaps in plastic surgery. Initial studies show that the imaging is capable of detecting the extent of perfusion of a given perforator once the flap is dissected and isolated on that single perforator. Selective clamping of the flap as a method for choosing the best perforator may prove to be difficult to determine since other perforators will provide compensatory flow. Therefore, future work should focus on clamping all perforators of the flap, only allowing one perforator to provide oxygen at a time, to visualize the perforasome of each perforator on an individual basis. Finally, imaging the flap over the duration of the surgery can eventually allow for the determination of quantitative standards, where if the flap is ischemic for too long, the risk for failure is higher, or if the flap is not re-perfusing as quickly as expected, this may be indication of a

venous clot. Ultimately, quantifying clinical decisions and reducing the need for judgement and prior experience.

To make this imaging system more relevant for clinical surgery, future work should focus on obtaining chemically-encoded images quickly enough to avoid movement artifacts due to breathing. During each imaging session, the patient's breathing had to be held so that movement of their diaphragm would not affect the chemically encoded images, which are processed on a pixel-by-pixel basis. Furthermore, the surface curvature of flaps can significantly influence the $\%HbO_2$ values measured by the system, as seen in Figure 4.10. During each imaging session, the plastic surgeon was required to place towels under the flap to flatten it, increasing the amount of time needed to image. Solutions to increasing the speed of the imaging system and decreasing the influence of surface curvature will be discussed further in Chatper 6.

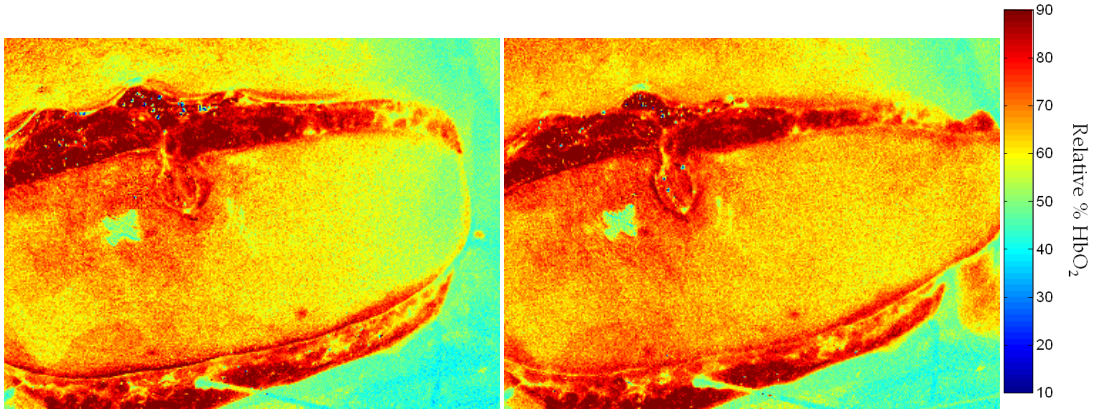

Figure 4.10 Effects of surface curvature on 3-shot hyperspectral imaging.

4.3. Lymphaticovenous Bypass Surgery

4.3.1. Overview & Surgical Problem

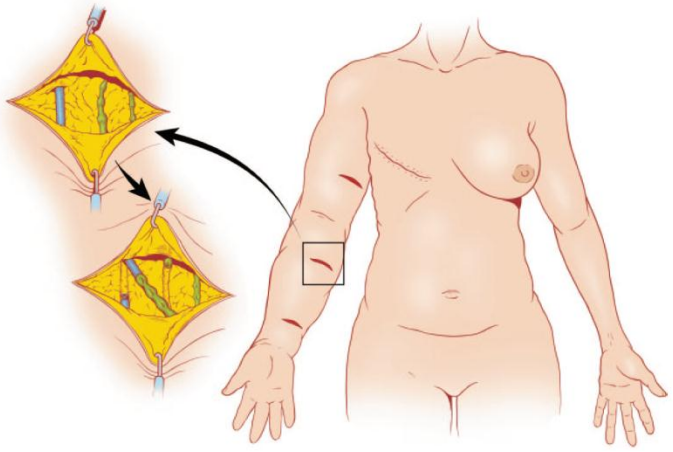

Figure 4.11 The concept behind a lymphaticovenous bypass surgery, where healthy lymphatic vessels (green) are anastomosed to the venous system (blue) to drain excess lymph fluid from the arm. [3]

During a mastectomy or lumpectomy surgery, patients undergo lymph node biopsy to determine the metastatic status of their cancer. One frequent complication of this biopsy is the severing or blockage of the lymphatic system between the upper arm and the rest of the body, resulting in a condition known as lymphedema. This blockage between the upper extremity and the superclavicular and subclavicular regions of the body results in the accumulation of lymph fluid in the arm due to the body's inability to clear the excess lymph. Upper arm lymphedema has a 42% incidence rate in women up to 5 years after breast cancer surgery. [41] Various treatments are available for patients to either combat the lymphedema on a day-to-day basis [42, 43] or to elect for a more permanent surgical solution. [44] Surgical procedures are available for patients whose medical treatment is ineffective, and they offer the option of a permanent solution by creating new channels for lymphatic fluid to drain and clear from the patient's arm. There is still debate on the optimal method for these lymphatic bypass surgeries, [3] however, all surgeons performing this operation face the challenge of finding healthy, large lymphatics to anastomose to their bypass channel as indicated in Figure 4.11. Lymphatics have no distinctive, visible color unless injected with a dye. Currently,

plastic surgeons "hunt" through the patient's lower arm to find these functional vessels using a lymphazerin blue dye. As they dissect the tissue there is always risk of inadvertent damage to functional lymph vessels, potentially exacerbating the patient's condition. There is a clear need for a less invasive method of identifying healthy lymphatics so that surgeons don't compromise the remaining viable tissue.

4.3.2. Methods

ICG fluorescence was employed using the Mid-Range DLP® imaging system in an attempt to find healthy lymphatic vessels in a non-invasive manner during lymphaticovenous bypass surgeries. 25 mg of IC-Green (Akorn Inc, Lake Forest, IL) was mixed with 10 mL of sterile aqueous solvent and was sub-dermally injected between the fingers of the patient's lymphedemous arm. The ICG solution was taken up by the lymphatic system and imaged following the injection.

As stated previously, ICG absorbs light differently in biological fluids due to protein binding. Therefore, the 815 ALP filter was fixed to the detector, instead of the 805 AELP filter, to block all incident light below λ = 815 nm. Furthermore, the OL490 light source was programmed to increase the excitation illumination cutoff by 10 nm from λ = 794.0 nm to λ = 804.2 nm with a 12.6 nm bandwidth to excite ICG at its absorption peak of λ = 805 nm in biological fluids. [20] Based on characterizations of the spot diameter and percent contrast, the spot diameter was reduced as much as reasonably possible to concentrate incident light on a smaller area of the patient's arm to create the most amount of contrast between the fluorophore and other biological tissues in the field of view. Raw fluorescence images were collected with detector, however, image subtraction using a dark background was not practical in the operating room since it required a pixel-to-pixel alignment of the entire field of view throughout the duration of the imaging session.

The 750 μm slit was also utilized in subsequent ICG imaging sessions to increase the amount of light power incident on the injected fluorophore. Similar imaging procedures were used such that

raw ICG fluorescence images were collected after injection of the ICG solution into the hand for viewing by the plastic surgeon.

4.3.3. Results & Discussion

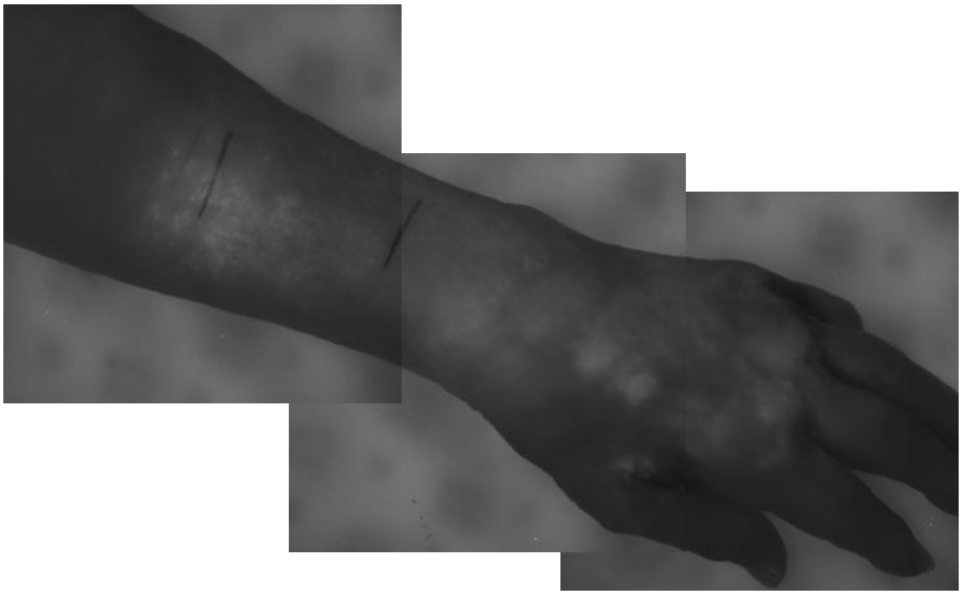

Figure 4.12 Raw fluorescence images of ICG using the 350 μm slit

A collage of raw fluorescence images can be seen in Figure 4.12, where ICG was injected inter-digitally in the lymphedemous arm. The contrast between ICG and normal tissue was not enough to distinguish lymphatic vessels in the patient's arm using the 350 μm slit. Therefore, the 750 μm slit was employed on following patients and a collage of raw fluorescence images using the 750 μm slit can be seen in Figure 4.13.

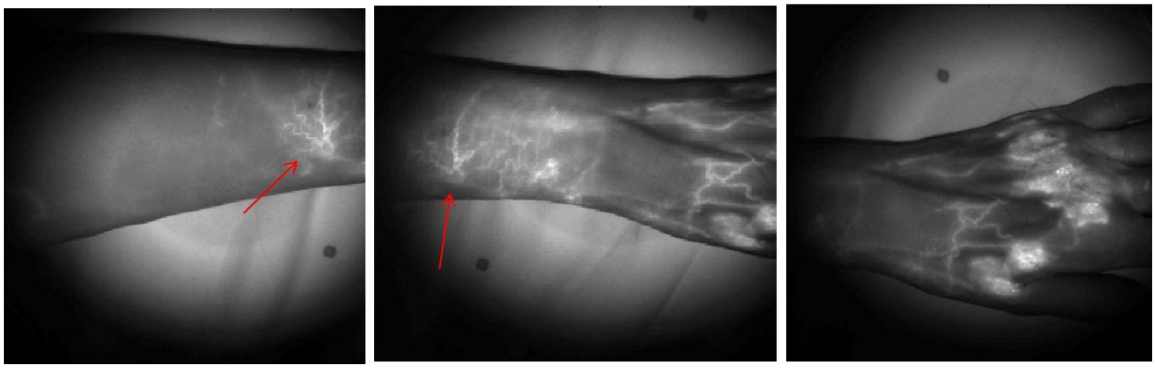

Figure 4.13 Raw fluorescence images of ICG using the 750 μm slit. Healthy lymphatic vessels to be used in the bypass surgery were successfully detected and are indicated by the red arrows.

The contrast between the fluorophore and surrounding tissue greatly improved with the 750 μm slit, and the plastic surgeon was able to successfully identify healthy lymphatic vessels, indicated by red arrows, for use in the bypass procedure.

4.3.4. Conclusions & Future Work

Fluorescence imaging of ICG was proven to be successful using the Mid-Range DLP® imaging system by maximizing the amount of light power coming out of the OL490 source. Focusing the incident light on a smaller viewing area, combined with the increased power of incident light made ICG fluorescence efficient enough to detect significant differences between the fluorophore and surrounding tissue.

Future work should focus on enhancing the contrast of ICG fluorescence utilizing the capabilities of the OL490. For instance, a standard reflectance image can be captured easily by programming the OL490 light source to illuminate with all wavelengths of light. This would allow NIR wavelengths of light to pass through the detector's filter, allowing the camera to capture a reflectance image without ICG fluorescence. The reflectance image, if taken immediately after a fluorescence image, can then be subtracted from the fluorescence image to obtain even greater contrast, and reduce the need for focused, more powerful light. Furthermore, it is clear that the apparent extinction coefficient of ICG (ε_{ICG}) changes with concentration, as indicated in Figure 2.20.

Therefore, it would be prudent to better control the concentration of the injected fluorophore so that its concentration reaches approximately 0.08 mg/mL, the theoretical concentration where maximum absorption occurs.

CHAPTER 5

CONCLUSIONS & FUTURE WORK

Overall, this thesis has characterized a multimodality DLP®-based imaging system and shown its utility *in vivo* in human clinical surgery for both hyperspectral and fluorescence imaging. Therefore, the research hypothesis that the Mid-Range DLP® imaging system can successfully incorporate multiple imaging modalities into one system by employing both hyperspectral imaging and fluorescence angiography to aid plastic surgeons in breast reconstruction surgery can be accepted. The imaging system is capable of producing continuous or non-continuous spectra with bandwidths as small as 7.5 nm and with as much power as 173.4 mW. It is capable of imaging regions of interest as small as 1.75" in diameter to 18" in diameter from a distance of 2 ft. at a rate of 1 fps with a resolution of 1,024 x 1,024 pixels. Furthermore, the system is capable of visualizing changes in tissue oxygenation using 3-shot hyperspectral imaging in free skin flap breast reconstruction surgery as well as lymphatic structures using ICG fluorescence in lymphaticovenous bypass surgery.

Although the system is capable of collecting these images, future work should focus on increasing the speed of data collection to make the system viable for industrial application. Currently, with the Mid-Range DLP® imaging system, the PIXIS 1024BR camera significantly limits speed due to the slow digitization of detected light. This camera was used because it has a CCD chip that is sensitive to NIR wavelengths of light, however, future improvements to this system should focus on obtaining a camera with similar spectral sensitivity, but much faster digitization. Furthermore, image acquisition speed could be significantly increased by increasing the light power coming out of the OL490 Agile Light Source. Currently, the source employs a 500W lamp which ultimately outputs a maximum of 173.4 mW using the largest slit with all mirrors on. With more light, the detector of the

imaging system would not need to be exposed as long, allowing for faster collection of data. Also, the OL490 ALS has significantly decreased output intensity in the NIR wavelengths. DLP® DMDs were first optimized for reflection of visible light in cinema projectors and may not be optimized to reflect NIR light.

To improve image quality, cross-polarization of the light source and camera detector would eliminate specular reflections that are common to biological tissues. Although this was handled by bringing detector counts to just below saturation such that specular reflections would show up as saturated pixels, cross-polarization should significantly improve image quality and may not require the detectors to have such high image counts before data collection can proceed. Furthermore, surface curvature is a big consideration when looking at large regions of interest. Kainerstorfer et. al. came up with a method which corrects for curvature in multispectral and hyperspectral data even after it has been collected. [45] However, the technique will only work for curvature angles ≤ 35°, and it requires an imaging system that utilizes cross-polarization, since specular reflections could create errors in the flattening of a surface.

Finally, although the hyperspectral imaging system is sensitive to changes in tissue oxygenation, the changes are relative to each patient and have not been absolutely quantified. For instance, patients with different melanin content in their skin may show similar changes in tissue oxygenation due to surgical intervention, but the absolute quantitative values will be different from patient to patient because of the absorption of other chromophores like melanin.

Overall this imaging system was designed, using the DLP® DMD as a tool, to bring together multiple imaging modalities into a single, integrated system for clinical surgery. The DLP® Mid-Range imaging system aims to quantify clinical decisions, minimizing the necessity for clinical judgement and prior experience, and enhancing the quality and safety of patient care.

REFERENCES

1. Jemal A, Bray F, Center MM, Ferlay J, Ward E, Forman D. Global Cancer Statistics. *CA: A Cancer Journal for Clinicians*. March/April 2011;61(2):69-90.

2. National Cancer Institute. Breast Cancer Treatment (PDQ) - National Cancer Institute. *National Cancer Institute at the National Institutes of Health*. July 20, 2011. Available at: http://www.cancer.gov/cancertopics/pdq/treatment/breast/Patient/page5 . Accessed August 1, 2011.

3. Suami H, Chang DW. Overview of Surgical Treatments for Breast Cancer-Related Lymphedema. *Plastic & Reconstructive Surgery*. December 2010;126(3):1853-1863.

4. Fox IJ, Brooker LGS, Heseltine W, Essex HE, Wood EH. A Tricarbocyanine dye for Continuous Recording of Dilution Curves in Whole Blood Independent of Variations in Blood Oxygen Saturation. *Procedures of Mayo Clinic*. 1957;32:478-484.

5. Vogel A, Venugopalan V. Mechanisms of Pulsed Laser Ablation of Biological Tissues. *Chemical Reviews*. February 2003;103(2):2003.

6. Benson RC, Kues HA. Fluorescence Properties of Indocyanine Green as Related to Angiography. *Physics in Medicine & Biology*. 1978;23(1):159-163.

7. Kogure K, David NJ, Yamanouchi U, Choromokos E. Infrared Absorption Angiography of the Fundus Circulation. *Archives of Ophthalmology*. 1970;83:209-214.

8. Gandorfer A, Messmer EM, Ulbig MW, Kampik A. Indocyanine Green Selectively Stains the Internal Limiting Membrane. *American Journal of Ophthalmology*. 2001;131:387-388.

9. Holm C. Clinical Applications of ICG Fluorescence Imaging in Plastic and Reconstructive Surgery. *The Open Surgical Oncology Journal*. 2010;2:37-47.

10. Taggart DP, Choudhary B, Anastasiadis K, Abu-Omar Y, Balacumaraswami L, Pigott DW. Preliminary Experience With a Novel Intraoperative Fluorescence Imaging Technique to Evaluate the Patency of Bypass Grafts in Total Arterial Revascularization. *Annals of Thoracic Surgery*. 2003;75:870-873.

11. Ogata F, Narushima M, Mihara M, Azuma R, Morimoto Y, Koshima I. Intraoperative Lymphography Using Indocyanine green Dye for Near-Infrared Fluorescence Labeling in Lymphedema. *Annals of Plastic Surgery*. August 2007;59(2):180-184.

12. Unno N, Inuzuka K, Suzuki M, et al. Preliminary Experience with a Novel Fluorescence Lymphography Using Indocyanine Green in Patients with Secondary Lymphedema. *Journal of Vascular Surgery*. May 2007;45(5):1016-1021.

13. Keller A. A New Diagnostic Algorithm for Early Prediction of Vascular Compromise in 208 Microsurgical Flaps Using Tissue Oxygen Saturation Measurements. *Annals of Plastic Surgery*. May 2009;62(5):538-543.

14. Althuis MD, Dozier JM, Anderson WF, Devesa SS, Brinton LA. Global Trends in Breast Cancer Incidence and Mortality, 1973-1997. *International Journal of Epidemiology*. February 2005;34:405-412.

15. Francis RP. *DLP Hyperspectral Imaging for Surgical and Clinical Utility*: University of Texas at Arlington Master's Thesis; 2009.

16. Zuzak KJ, Francis RP, Wehner EF, Litorja M, Cadeddu JA, Livingston EH. Active DLP Hyperspectral Illumination: A Noninvasive, In Vivo, System Characterization Visualizing Tissue Oxygenation at Near Video Rates. *Analytical Chemistry*. August 2011;83:7424-7430.

17. Thapa A. *Post-Operative Renal Function Analysis Using Visible DLP(R) Hyperspectral Imaging System*: University of Texas at Arlington Master's Thesis; 2010.

18. Fong A, Bronson B, Wachman E. Advanced Photonic Tools for Hyperspectral Imaging in the Life Sciences. *SPIE Newsroom*. April 2008.

19. Hornbeck LJ. Digital Light Processing for High-Brightness High-Resolution Applications. Paper presented at: Proceedings of SPIE, 1997; San Jose.

20. Landsman MLJ, Kwant G, Mook GA, Zijlstra G. Light-Absorbing Properties, Stability, and Spectral Stabilization of Indocyanine Green. *Journal of Applied Physiology*. 1976;4(40):575-583.

21. Haritglou C, Gandorfer A, Chaumberger M, Tadayoni R, Kampik A. Light-Absorbing Properties of Indocyanine Green Depending on Concentration and Solvent Medium. *Investigative Ophthalmology & Visual Science*. June 2003;44(6):2722-2729.

22. Sony ILX511 Datasheet. *Ocean Optics*. http://www.oceanoptics.com/technical/detectorsonyILX511.pdf . Accessed November 17, 2010.

23. Hecht E. *Optics*. 4th ed. San Francisco: Addison Wesley; 2002.

24. Zuzak KJ, Francis RP, Wehner EF, et al. DLP Hyperspectral Imaging for Surgical and Clinical Utility. *SPIE*. 2009;7210(06):1-9.

25. Tracy CR, Terrell JD, Francis RP, et al. Characterization of Renal Ischemia Using DLP Hyperspectral Imaging: A Pilot Study Comparing Artery-Only Occlusion Versus Artery and Vein Occlusion. *Journal of Endourology*. March 2010;24(3):321-325.

26. Wehner E, Thapa A, Livingston E, Zuzak K. NIR DLP Hyperspectral Imaging System for Medical Applications. *Proceedings of SPIE*. January 2011;7932(04):1-9.

27. Tsai BK, Allen DW, Hanssen LM, Wilthan B, Zeng J. A Comparison of Optical Properties Between High Density and Low Density Sintered PTFE. *Proceedings of SPIE*. 2008;7065(0Y):1-9.

28. Zuzak KJ, Schaeberle MD, Lewis EN, Levin IW. Visible Reflectance Hyperspectral Imaging: Characterization of a Noninvasive, In Vivo System for Determining Tissue Perfusion. *Analytical Chemistry*. May 2002;74(9):2021-2028.

29. Best SL, Holzer MS, Jackson N, et al. Assessment of Renal Oxygenation During Partial Nephrectomy Using DLP Hyperspectral Imaging. *Proceedings of SPIE*. 2011;7932(02):1-8.

30. Best SL, Thapa A, Holzer MJ, et al. Minimal Arterial In-flow Protects Renal Oxygenation and Function During Porcine Partial Nephrectomy: Confirmation by Hyperspectral Imaging. *Urology*. October 2011;78(4):961-966.

31. Hebden JC, Arridge SR, Delpy DT. Optical Imaging in Medicine: I. Experimental Techniques. *Physics in Medicine and Biology*. 1997;42:825-840.

32. Hariharan S. *Surgical Fluorescence Imager for Visualizing Anteriorly Placed Biliary Structures, In Vivo, During Human Cholecystectomy*. Arlington: University of Texas at Arlington; 2008.

33. Mangum ML, Saint-Cyr M, Wehner EF, Thapa A, Livingston E, Zuzak KJ. Visible to NIR DLP Hyperspectral Imaging System for Surgical Utility Using Inherent Chromophores and Fluorescent Probes. *Proceedings of SPIE*. February 2011;7932(03):1-11.

34. International Electrotechnical Commission. *Photobiological Safety of Lamps and Lamp Systems*: IHS; 2006. 62471.

35. American Society of Plastic Surgeons. *American Society of Plastic Surgeons Report of the 2010 Plastic Surgery Statistics*. Arlington Heights: American Society of Plastic Surgeons; 2010. Report of the 2010 Plastic Surgery Statistics.

36. Allen RJ, Treece P. Deep Inferior Epigastric Perforator Flap for Breast Reconstruction. *Annals of Plastic Surgery*. January 1994;32(1):32-38.

37. Bailey SH, Saint-Cyr M, Wong C, et al. The Single Dominant Medial Row Perforator DIEP Flap in Breast Reconstruction: Three Dimensional Perforasome and Clinical Results. *Plastic and Reconstructive Surgery*. September 2010;126(3):739-751.

38. Wong C, Saint-Cyr M, Mojallal A, et al. Perforasomes of the DIEP Flap: Vascular Anatomy of the Lateral Versus Medial Row Perforators and Clinical Implications. *Plastic & Reconstructive Surgery*. March 2010;125(3):772-782.

39. Wong C, Saint-Cyr M, Arbique G, et al. Three- and Four-Dimensional Computed Tomography Angiographic Studies of Commonly Used Abdominal Flaps in Breast Reconstruction. *Plastic & Reconstructive Surgery*. July 2009;124(1).

40. Saint-Cyr M, Wong C, Schaverien M, Mojallal A, Rohrich RJ. The Perforasome Theory: Vascular Anatomy and Clinical Implications. *Plastic and Reconstrucive Surgery*. May 2009;124(5):1529-1544.

41. Norman SA, Localio AR, Potashnik SL, et al. Lymphedema in Breast Cancer Survivors: Incidence, Degree, Time Course, Treatment, and Symptoms. *Journal of Clinical Oncology*. January 2009;27(3):390-397.

42. Badger CMA, Peacock JL, Mortimer PS. A Randomized, Controlled, Parallel-Group Clinical Trial Comparing Multilayer Bandaging Followed by Hosiery Versus Hosiery Alone in the Treatment of Patients with Lymphedema of the Limb. *Cancer*. June 2000;88(12):2832-2837.

43. Szuba A, Cooke JP, Yousuf S, Rockson SG. Decongestive Lymphatic Therapy for Patients with Cancer-Related or Primary Lymphedema. *The American Journal of Medicine*. September 2000;109(4):296-300.

44. Campisi C, Davini D, Bellini MD, et al. Lymphatic Microsurgery for the Treatment of Lymphedema. *Microsurgery*. 2006;26(1):65-69.

45. Kainerstorfer JM, Amyot F, Ehler M, et al. Direct Curvature Correction for Noncontact Imaging Modalities Applied to Multispectral Imaging. *Journal of Biomedical Optics*. July/August 2010;15(4):046013-1-14.

46. World Health Organization. *The Global Burden of Disease: 2004 Update*. Geneva: WHO Press; 2008.

47. Jemal A, Center MM, Desantis C, Ward EM. Global Patterns of Cancer Incidence and Mortality Rates and Trends. *Cancer Epidemiology, Biomarkers & Prevention*. July 2010;19:1893-1907.

48. Goldberg JA, Scott RN, Davidson PM, et al. Psychological Morbidity in the FIrst Year after Breast Surgery. *European Journal of Surgical Oncology*. August 1992;18(4):327-331.

49. Andrade WN, Baxter N, Semple JL. Clinical Determinants of Patient Satisfaction with Breast Reconstruction. *Plastic and Reconstructive Surgery*. January 2001;107(1):46-54.

50. Zuzak KJ, Naik SC, Alexandrakis G, Hawkins D, Behbehani K, Livingston EH. Characterization of a Near-Infrared Laparoscopic Hyperspectral Imaging System for Minimally Invasive Surgery. *Analytical Chemistry*. June 2007;79(12):4709-4715.

51. Pestana IA, Coan B, Erdmann D, Marcus J, Levin LS, Zenn MR. Early Experience with Fluorescent Angiography in Free-Tissue Transfer Reconstruction. *Plastic and Reconstructive Surgery*. April 2009;123(4):1239-1244.

52. Hulka BS, Moorman PG. Breast Cancer: Hormones and Other Risk Factors. *Maturitas*. 2001;38:103-116.

53. Key J, Hodgson S, Omar RZ, et al. Meta-Analysis of Studies of Alcohol and Breast Cancer with Consideration of the Metholdological Issues. *Cancer Causes Control*. 2006;17:759-770.

54. Hopwood P. The Assessment of Body Image in Cancer Patients. *European Journal of Cancer*. 1993;29(2):276-281.

55. Harcout D. Psychological Aspects of Breast Reconstruction: A Review of the Literature. *Integrative Literature Reviews and Meta-Analyses*. May 2001;35(4):477-487.

56. Harcourt DM, Rumsey NJ, Ambler NR, et al. The Psychological Effect of Mastectomy with or without Breast Reconstruction: A Prospective, Multicenter Study. *Plastic and Reconstructive Surgery*. March 2003;111(3):1060-1068.

57. Parker PA, Youssef A, Walker S, et al. Short-Term and Long-Term Psychosocial Adjustment and Quality of Life in Women Undergoing Different Surgical Procedures for Breast Cancer. *Annals of Surgical Oncology*. June 2007;14(11):3078-3089.

58. Al-Ghazal SK, Fallowfield L, Blamey RW. Comparison of Psychological Aspects and PatientSatisfaction Following Breast Conserving Surgery, Simply Mastectomy and Breast Reconstruction. *European Journal of Cancer*. 2000;36:1938-1943.

59. Sistrunk WE. Contribution to Plastic Surgery: Removal of Scars by Stages; An Open Operation for Extensive Laceration of the Anal Sphincter; The Konkoleon Operation for Elephantiasis. *Annals of Surgery*. February 1927;85(2):185-193.

60. Thompson N. Buried Dermal Flap Operation for Chronic Lymphedema of the Extremities. *Plastic & Reconstructive Surgery*. June 1970;45(6):541-554.

61. O'Brien BM, Khazanchi RK, Kumar PAV, Dvir E, Pederson WC. Liposuction in the Treatment of Lymphoedema; A Preliminary Report. *British Journal of Plastic Surgery*. September 1989;42(5):530-533.

62. Frick A, Hoffmann JN, Baumeister RGH, Putz R. Liposuction Technique and Lymphatic Lesions in LowerLegs:AnatomicStudy to Reduce Risks. *Plastic & Reconstructive Surgery*. June 1999;103(7):1868-1873.

63. Hortobagyi GN. Treatment of Breast Cancer. *New England Journal of Medicine*. October 1998;339(14):974-984.

BIOGRAPHICAL INFORMATION

Michael Mangum has always had an interest in helping others within the field of healthcare since his first experiences working in a hospital as a Patient Care Assistant in 2005. As an undergraduate in 2004, he pursued the Pre-Medicine track at Texas Christian University, but decided to eschew more traditional majors like biology and chemistry, with the understanding that medical school would provide all the biochemical knowledge he could ever want to know. As a result, he stumbled upon mechanical engineering and learned how to apply mathematics to explain the physical world. The engineering program at TCU also provided an environment that fostered his innovative thinking, teamwork, and leadership skills. He continued to pursue medical school; however, after being waitlisted at multiple medical schools in Texas, it was time to look elsewhere. Michael began the Joint Biomedical Engineering Program at the University of Texas at Arlington and the University of Texas Southwestern Medical Center in the fall of 2009 and has enjoyed applying engineering principles to the field of medicine. His classwork has mostly been focused on the field of biomaterials and tissue engineering; however, he has also gained valuable research experience developing imaging systems, working with surgeons at UT Southwestern, and interning at an Austin-based company, Digital Light Innovations. After graduating from the program in 2011, Michael plans to gain experience in industry to apply what he has learned and to fulfill his goals of applying and translating new technologies to solve healthcare-related problems.